A model-based simulation framework for coupled acoustics, elastodynamics, and damage with application to nano-pulse lithotripsy

Yangyuanchen Liu [a], Pei Zhong [a], Oscar Lopez-Pamies [b], John E. Dolbow [a,*]

[a] *Department of Mechanical Engineering and Materials Science, Duke University, Durham, NC 27707, USA*
[b] *Department of Civil and Environmental Engineering, University of Illinois at Urbana–Champaign, IL 61801, USA*

ARTICLE INFO

ABSTRACT

We develop a model for solid objects surrounded by a fluid that accounts for the possibility of acoustic pressures giving rise to damage on the surface of the solid. The propagation of an acoustic pressure in the fluid domain is modeled by the acoustic wave equation. On the other hand, the response of the solid is described by linear elastodynamics coupled with a gradient damage model, one that is based on a cohesive-type phase-field description of fracture. The interaction between the acoustic pressure and the deformation and damage of the solid are represented by transmission conditions at the fluid–solid interface. The resulting governing equations are discretized using a finite-element/finite-difference method that pays particular attention to the spatial and temporal scales that need to be resolved. Results from model-based simulations are provided for a benchmark problem as well as for recent experiments in nano-pulse lithotripsy. A parametric study is performed to illustrate how damage develops in response to the driving force (magnitude and location of the acoustic source) as a function of the fracture resistance of the solid. The results are shown to be qualitatively consistent with experimental observations for the location and size of the damage fields on the solid surface. A study of limiting cases also suggests that both the threshold for damage and the critical fracture energy are important to consider in order to capture the transition from damage initiation to complete localization. A low-cycle fatigue model is proposed that degrades the fracture resistance of the solid as a function of accumulated tensile strain energy, and it is shown to be capable of capturing damage localization in simulations of multi-pulse nano-pulse lithotripsy.

1. Introduction

The interaction of acoustic waves with damaged structures is of long-standing interest to the engineering and materials science communities. It is useful to understand how acoustic waves both interact with damaged structures but can also induce damage when they are sufficiently strong. Applications range from ultrasonic damage detection (Broda et al., 2014; Ebna Hai et al., 2019; Li and Zhou, 2019) to device protection (Chen et al., 2003; Barsoum, 2015; Li et al., 2015; Ramirez and Gupta, 2018). In this work, our focus concerns shock wave lithotripsy, a highly effective treatment for the removal of kidney stones (Lingeman et al., 2009; Weinberg and Ortiz, 2009; Zhong, 2013; Zhang et al., 2017; Yang, 2018; Zhang et al., 2019). Although the interaction of a surface acoustic wave with nominally elastic solids has been studied both experimentally and theoretically (Zhang et al., 2017; Yang, 2018; Zhang et al., 2019), the manner in which damage develops on the surface of the structure has yet to be understood. In this work, we take advantage of recent developments in gradient-damage models to develop a fully coupled formulation for acoustics, linear elastodynamics, and damage. We then use model-based simulations to examine the extent to which this formulation can explain recent experimental observations.

Among the applications of acoustic-induced damage, shock wave lithotripsy is a medical procedure used to treat kidney (as well as gall-bladder and pancreatic) stones in patients. Roughly speaking, lithotripsy – which literally means "crushing" (tripsy) "stones" (lithos) – refers to the process of breaking up kidney stones that are too large for patients to pass on their own. This can be effected in a number of ways, with perhaps the most common approach at present being the so-called extracorporeal shock wave lithotripsy (ESWL) (Kaplan et al., 2016). As its name suggests, this is a non-invasive procedure that consists in the administration of shock waves aimed at the stones. Here the phrase "shock waves" describes the high-energy acoustical waves that are generated during lithotripsy, not to be confused with shocks that form during supersonic flow, for example. While there is no doubt

---

* Corresponding author.
  E-mail address: john.dolbow@duke.edu (J.E. Dolbow).

that ESWL has been a success since its introduction in the 1980s, it is an expensive procedure and can sometimes result in collateral tissue damage.

Nano-pulse lithotripsy (NPL) is a relatively new intracorporeal approach wherein short electrical pulses discharged near the surface of a stone serve to fragment it efficiently. In NPL, a probe is placed within millimeters of the stone surface and generates a spark discharge that gives rise to a shock wave that propagates through the surrounding fluid and impacts the stone. The shock waves break up the stones through a dynamic process involving the contribution of various stress-waves propagating inside the stone and cavitation produced in the surrounding liquid medium.

However, several aspects of the treatment of kidney stones using shock waves are not completely understood, as discussed by Tanguay and Colonius (2003). Recently, Zhang et al. (2019) conducted a series of experiments and accompanying model-based simulations for NPL on glass samples that provided some key observations. The work of Zhang et al. (2019) focused on the interaction between the shock wave propagating through the surrounding fluid and the impedance mismatch with the solid sample, giving rise to a surface acoustic wave in the latter. The response of the system was examined as a function of the "standoff distance" between the probe tip and the glass surface. Importantly, the experiments indicated that the radii of the "ring-like" fractures increased with the standoff distance, while the width of the damaged region decreased.

Although some model-based simulations of shock-wave lithotripsy have been developed (Tham et al., 2007; Weinberg and Ortiz, 2009), relatively little work has focused on simulations of NPL. The simulations by Zhang et al. (2019) employed a model for coupled acoustics and linear elastodynamics, but without any explicit representation for the damage in the solid. There are some challenges to developing a robust computational framework to simulate acoustic-induced damage evolution in NPL. First of all, the shock wave treatment is a coupled acoustic-elastodynamics-damage problem, and the interactions between the propagation of the acoustic waves and the deformation of the stone need to be properly represented. Moreover, cracks form and propagate in response to the repeated shock waves. This shockwave-crack interaction has to be incorporated into the model and accompanying computational framework if model-based simulations have any chance at reproducing experimental observations.

In this work, we extend the model of Zhang et al. (2019) by coupling the fluid acoustics and solid elastodynamics to a cohesive-type phase-field model of fracture. Phase-field models for fracture originated some twenty years ago (Bourdin et al., 2000) as regularizations of the variational description of fracture introduced by Francfort and Marigo (1998), which is nothing more than the mathematical statement of Griffith's fracture postulate in its general form of energy cost–benefit analysis (Griffith, 1921). In these models, a phase field or order parameter is introduced to describe in a regularized manner the presence of sharp crack discontinuities within a continuum formulation. The particular version used in this work is a cohesive-type variation (Lorentz et al., 2011; Geelen et al., 2019) of the original phase-field model (Bourdin et al., 2000), which employs an energetic threshold to describe damage initiation in uniaxial tension and that has the merit of being insensitive to the regularization length.

The studies of Zhang et al. (2019) indicated that macroscale cracks did not form in some cases until a sufficient number of shocks were applied. For models relying on damage fields to represent sharp crack surfaces, this could manifest as a damage field that slowly accumulates with increasing shocks until reaching a critical level at which localization ensues. It is also plausible, however, that the shocks degrade the fracture resistance of the material in a manner that is more typical of low-cycle fatigue. Fatigue-based concepts have been introduced into gradient damage and variational fracture models following various approaches (Peerlings et al., 2000; da Costa Mattos, 2017; Alessi et al., 2018; Luo et al., 2020; Alessi and Ulloa, 2023). In this work, concepts
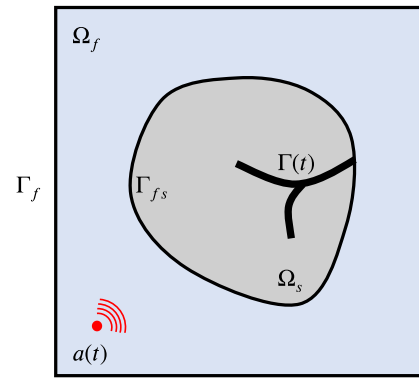

Fig. 1. Schematic of a coupled acoustics-elastodynamics-damage problem: a solid body Ω_s with a sharp crack discontinuity $\Gamma(t)$ is immersed in a fluid environment Ω_f, and interacts with the surrounding fluid through the fluid–solid interface Γ_{fs}.

from the recent fatigue model of Carrara et al. (2020) and Grossman-Ponemon et al. (2022) are adapted to degrade both the threshold for damage and the fracture toughness in order to simulate damage localization under multi-pulse NPL.

The paper is organized as follows. We begin in Section 2 by formulating the coupled acoustics, elastodynamics, and damage problem. This includes the governing equations in the fluid and the solid domains, as well as a description of the cohesive-type phase field model for fracture in the solid. In Section 3, we present the FE/FD (finite-element/finite-difference) discretization of the proposed coupled problem. Then, in Sections 4 and 5, we present a series of representative results from model-based simulations of a benchmark problem and of recent experimental studies of NPL. Finally, in Section 6, we provide a summary of the main findings of this work and record a number of concluding remarks.

2. Problem formulation

2.1. Initial configuration and kinematics

Consider a solid that in its initial configuration, at time $t = 0$, occupies the open domain Ω_s, with boundary $\partial\Omega_s$ and outward unit normal $\mathbf{n}$. As schematically depicted in Fig. 1, the solid is surrounded by a fluid occupying the domain Ω_f. We denote by Γ_f the outer boundary of the fluid domain and by Γ_{fs} the fluid–solid interface, so that $\partial\Omega_s = \Gamma_{fs}$ and $\partial\Omega_f = \Gamma_{fs} \cup \Gamma_f$.

Identify material points in both the solid and the fluid by their initial position vector $\mathbf{x} \in \Omega_s \cup \Omega_f$. In response to an acoustic source that is immersed in the fluid domain (to be described below), the position vector $\mathbf{x}$ of a material point may move to a new position specified by the mapping

$$\mathbf{y} = \mathbf{x} + \mathbf{u}(\mathbf{x}, t),$$

where $\mathbf{u}$ is the displacement field. Making use of standard notation, we write the displacement gradient and Lagrangian velocity fields at $\mathbf{x}$ and t as

$$\nabla\mathbf{u} = \frac{\partial\mathbf{u}}{\partial\mathbf{x}}(\mathbf{x}, t) \quad \text{and} \quad \dot{\mathbf{u}} = \frac{\partial\mathbf{u}}{\partial t}(\mathbf{x}, t).$$

Since the focus of this work is on nearly incompressible Newtonian fluids (e.g., water), on hard brittle solids (e.g., glass), and on externally applied acoustic point sources, we shall restrict attention to small-displacement kinematics throughout, both in the fluid as well as in the solid.
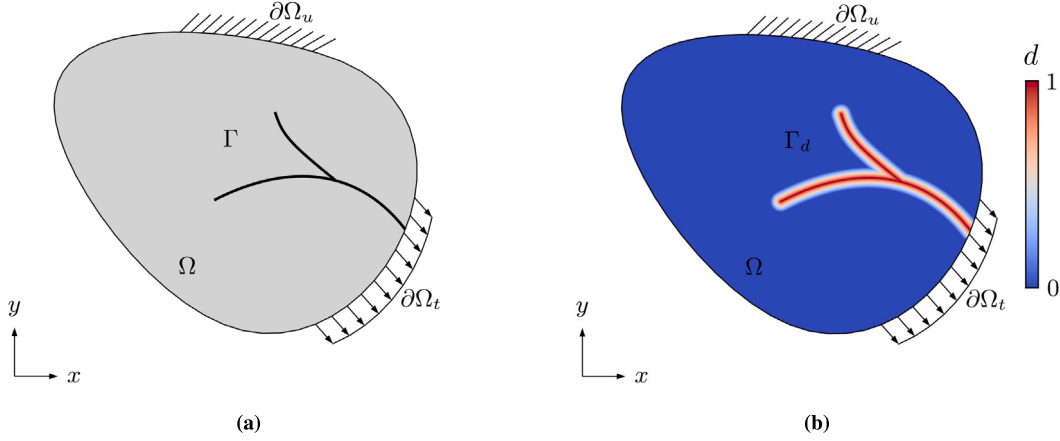
Fig. 2. (a) Sketch of a body, Ω, with an internal discontinuity Γ. (b) A regularization of the internal discontinuity, as represented by a scalar damage field d.

2.2. Acoustics in the fluid

Balance of linear and angular momenta. Making use of mass conservation and Cauchy's fundamental postulate, the balance of linear and angular momenta in the fluid read

$$\operatorname{div} \boldsymbol{T} + \boldsymbol{b}_f = \rho_f \ddot{\boldsymbol{u}}, \quad (\boldsymbol{x}, t) \in \Omega_f \times [0, T] \tag{1}$$

and

$$\boldsymbol{T}^T = \boldsymbol{T}, \quad (\boldsymbol{x}, t) \in \Omega_f \times [0, T], \tag{2}$$

respectively, where ρ_f stands for the initial mass density of the fluid, $\boldsymbol{b}_f$ is a body force per unit initial volume, $\boldsymbol{T}$ is the Cauchy stress tensor, and div stands for the standard divergence operator, that is, in indicial notation, $(\operatorname{div} \boldsymbol{T})_i = \partial T_{ij}/\partial x_j$.

Constitutive behavior of the fluid. The mechanical behavior of the fluid is modeled as a linear elastic fluid (Wang and Truesdell, 1973). Accordingly, the Cauchy stress tensor at any material point $\boldsymbol{x} \in \Omega_f$ and time $t \in [0, T]$ is given by the constitutive relation

$$\boldsymbol{T}(\boldsymbol{x}, t) = -p\boldsymbol{I} \quad \text{with} \quad p = -K_f \operatorname{div} \boldsymbol{u}, \tag{3}$$

where the material constant K_f denotes the bulk modulus of the fluid.

Note that the constitutive relation (3) satisfies automatically the balance of angular momentum (2). Substitution of the constitutive relation (3) in the balance of linear momentum (1) leads to

$$-\nabla p + \boldsymbol{b}_f = \rho_f \ddot{\boldsymbol{u}}, \quad (\boldsymbol{x}, t) \in \Omega_f \times [0, T]. \tag{4}$$

Taking the divergence of this last equation leads in turn to

$$-\Delta p + a = \rho_f \operatorname{div} \ddot{\boldsymbol{u}}, \quad (\boldsymbol{x}, t) \in \Omega_f \times [0, T], \tag{5}$$

where we have made use of the notation $a = \operatorname{div} \boldsymbol{b}_f$. Finally, recognizing from (3) that

$$\ddot{p} = -K_f \operatorname{div} \ddot{\boldsymbol{u}}$$

allows Eq. (5) to be rewritten in the form

$$\Delta p - \frac{1}{c_f^2} \ddot{p} = a, \quad (\boldsymbol{x}, t) \in \Omega_f \times [0, T], \tag{6}$$

where the material constant $c_f := \sqrt{K_f/\rho_f}$ is the speed of propagation of acoustic waves in the fluid. Eq. (6) is nothing more than the acoustic wave equation; see, e.g., Kinsler et al. (1999).

In the sequel, we shall consider that the fluid is subjected to an acoustic point source

$$a(\boldsymbol{x}, t) = S_0(t)\delta(\boldsymbol{x} - \boldsymbol{x}_s),$$

where $S_0(t)$ is the strength of the source and $\delta(\boldsymbol{x} - \boldsymbol{x}_s)$ is the Dirac delta function centered at position $\boldsymbol{x}_s$. We shall also consider that the fluid

domain is initially at rest and stress free, while its outer boundary is traction free:

$$p(\boldsymbol{x}, 0) = 0, \quad \dot{p}(\boldsymbol{x}, 0) = 0, \quad \boldsymbol{x} \in \Omega_f, \quad \text{and}$$

$$\nabla p \cdot \boldsymbol{n} = 0, \quad (\boldsymbol{x}, t) \in \Gamma_f \times [0, T]. \tag{7}$$

2.3. Elastodynamics and damage in the solid

Balance of linear and angular momenta. Making use again of mass conservation and Cauchy's fundamental postulate, much like in the fluid domain, the balance of linear and angular momenta in the solid read

$$\operatorname{div} \boldsymbol{\sigma} + \boldsymbol{b}_s = \rho_s \ddot{\boldsymbol{u}}, \quad (\boldsymbol{x}, t) \in \Omega_s \times [0, T] \tag{8}$$

and

$$\boldsymbol{\sigma}^T = \boldsymbol{\sigma}, \quad (\boldsymbol{x}, t) \in \Omega_s \times [0, T], \tag{9}$$

where ρ_s stands for the initial mass density of the solid, $\boldsymbol{b}_s$ is a body force per unit initial volume, and, in keeping with classical notation, we have used $\boldsymbol{\sigma}$ (instead of $\boldsymbol{T}$) to denote the Cauchy stress tensor.

Constitutive behavior of the solid. In response to mechanical forces, the solid can either deform elastically and/or fracture. We model the elastic behavior as linear and isotropic. The fracture behavior, we model in a regularized manner in terms of a phase field

$$d = d(\boldsymbol{x}, t), \quad (\boldsymbol{x}, t) \in \Omega_s \times [0, T],$$

taking values in the range $[0, 1]$. The value $d = 0$ identifies the intact regions of the solid and $d = 1$ those that have been fractured, while the transition from $d = 0$ to $d = 1$ is set to occur smoothly over regions of small thickness of regularization length scale ℓ; see Fig. 2 for a schematic.

In this setting, we take the Cauchy stress tensor $\boldsymbol{\sigma}$ at any material point $\boldsymbol{x} \in \Omega_s$ and time $t \in [0, T]$ to be given by the constitutive relation

$$\boldsymbol{\sigma}(\boldsymbol{x}, t) = g(d)\frac{\partial \psi^+}{\partial \boldsymbol{\varepsilon}}(\boldsymbol{\varepsilon}(\boldsymbol{u})) + \frac{\partial \psi^-}{\partial \boldsymbol{\varepsilon}}(\boldsymbol{\varepsilon}(\boldsymbol{u})) \quad \text{with}$$

$$\begin{cases} \psi^+(\boldsymbol{\varepsilon}) = \mu\left(\boldsymbol{\varepsilon}^+ \cdot \boldsymbol{\varepsilon}^+\right) + \frac{\lambda}{2}\langle \operatorname{tr} \boldsymbol{\varepsilon}\rangle_+^2 \\ \psi^-(\boldsymbol{\varepsilon}) = \mu\left(\boldsymbol{\varepsilon}^- \cdot \boldsymbol{\varepsilon}^-\right) + \frac{\lambda}{2}\langle \operatorname{tr} \boldsymbol{\varepsilon}\rangle_-^2 \end{cases}. \tag{10}$$

In these expressions, μ and λ stand for the Lamé constants,

$$\boldsymbol{\varepsilon}(\boldsymbol{u}) = \frac{1}{2}\left(\nabla \boldsymbol{u} + \nabla \boldsymbol{u}^T\right) = \sum_{a=1}^{3} \varepsilon_a \boldsymbol{n}_a \otimes \boldsymbol{n}_a$$

is the (infinitesimal) strain tensor, with ε_a and $\boldsymbol{n}_a \otimes \boldsymbol{n}_a$ denoting its eigenvalues and corresponding eigentensors,

$$\varepsilon^+ = \sum_{a=1}^{3} \langle \varepsilon_a \rangle_+ \, \boldsymbol{n}_a \otimes \boldsymbol{n}_a \quad \text{and} \quad \varepsilon^- = \sum_{a=1}^{3} \langle \varepsilon_a \rangle_- \, \boldsymbol{n}_a \otimes \boldsymbol{n}_a, \quad \text{with}$$

$$\langle x \rangle_\pm := \frac{|x| \pm x}{2},$$

are the "tensile" and "compressive" parts of the strain tensor (Miehe et al., 2010), and $g(d)$ is the so-called degradation function.

In this work, we make use of the rational function proposed in Lorentz et al. (2011) and Lorentz (2017) for the degradation function $g(d)$, namely,

$$g(d) = \frac{(1-d)^2}{(1-d)^2 + \dfrac{3\mathcal{G}_c}{8\ell\psi_c}(1+d)d}, \tag{11}$$

where the material constant $\mathcal{G}_c$ denotes the critical energy release rate of the solid, while the parameter ψ_c is a nucleation energy that describes a threshold for damage evolution. Given a uniaxial tensile strength σ_{ts} for the solid of interest, a simple means to estimate the nucleation energy ψ_c in (11) is to consider the strain energy for a sample in uniaxial tension. The nucleation energy can then be approximated as

$$\psi_c \approx \frac{\sigma_{ts}^2}{2E}.$$

where $E = ((2\mu + 3\lambda)\mu)/(\mu + \lambda)$ is the Young's modulus of the solid.

Remark. Importantly, the use of the degradation function (11) ensures that the threshold for damage is insensitive to the choice of regularization length ℓ. The regularization length does, however, have an upper bound that depends on the values of $\mathcal{G}_c$ and ψ_c as given by Lorentz et al. (2011) and Geelen et al. (2019)

$$\ell \leq \frac{\mathcal{G}_c}{8\psi_c}.$$

It bears emphasis that this regularization length turns out to be slightly smaller than a physical length scale for the material, namely the *characteristic length* of the fracture process zone size in Mode I, given by

$$\ell_{ch} = \frac{E'\mathcal{G}_c}{\sigma_{ts}^2},$$

where $E' = E$ in three dimensions and plane stress, and $E' = E/(1-\nu)$ in plane strain; see, e.g., Rice (1980), Hillerborg et al. (1976).

Evolution equation for the phase field d. The next step in the formulation of the elastodynamics and damage in the solid is to describe how the phase field d evolves in time as the solid is subjected to mechanical forces.

Consistent with the evolution that results from the phase-field regularization of the variational approach to fracture (Francfort and Marigo, 1998; Bourdin et al., 2008) for the so-called AT-1 approximation (Ambrosio and Tortorelli, 1990, 1992), we consider

$$\begin{cases} \text{div} \left[\ell\mathcal{G}_c \nabla d \right] = \dfrac{4}{3} g'(d)\psi^+(\varepsilon(\boldsymbol{u})) + \dfrac{\mathcal{G}_c}{2\ell}, & \text{if } d(\boldsymbol{x},t) > 0, \quad (\boldsymbol{x},t) \in \Omega_s \times [0,T] \\ \text{div} \left[\ell\mathcal{G}_c \nabla d \right] \leq \dfrac{4}{3} g'(d)\psi^+(\varepsilon(\boldsymbol{u})) + \dfrac{\mathcal{G}_c}{2\ell}, & \text{if } d(\boldsymbol{x},t) = 0, \quad (\boldsymbol{x},t) \in \Omega_s \times [0,T] \end{cases}, \tag{12}$$

where $g' = \mathrm{d}g/\mathrm{d}d$ and where we remark that the inequalities in these expressions embody the classical assumption that fracture is a purely dissipative and irreversible process.

Remark. The evolution Eq. (12) has the merit of describing the nucleation of fracture from large pre-existing cracks as well as the propagation of cracks in a manner that is consistent with the Griffith energy competition.

Remark. Under states of uniform stress of the "tensile" diagonal form $\sigma = \text{diag}(\sigma_1 \geq 0, \sigma_2 \geq 0, \sigma_3 \geq 0)$, the evolution Eq. (12) predicts nucleation of fracture whenever the algebraic equation

$$\mathcal{F}(\boldsymbol{\sigma}) = \frac{J_2}{\mu} + \frac{I_1^2}{9\kappa} - \frac{\sigma_{ts}^2}{E} = 0 \tag{13}$$

is satisfied, where $\kappa = \lambda + 2\mu/3$ is the bulk modulus of the solid, $I_1 = \text{tr}\,\boldsymbol{\sigma} = \sigma_1 + \sigma_2 + \sigma_3$, and $J_2 = \text{tr}[\boldsymbol{\sigma} - (\text{tr}\,\boldsymbol{\sigma})/3\,\boldsymbol{I}]/2 = (\sigma_1^2 + \sigma_2^2 + \sigma_3^2 - \sigma_1\sigma_2 - \sigma_1\sigma_3 - \sigma_2\sigma_3)/3$. In other words, the surface (13) in stress space is the strength surface predicted by the evolution Eq. (12). It happens to be identical to the strength surface predicted by the original AT-1 phase-field model (*cf.* Eq. (8) in Kumar et al. (2020)). As a result, it shares the same limitations as the original model (see Section 3 in Kumar et al. (2020)), save for one, its predicted strength surface (13) is independent of the choice of regularization length ℓ. In spite of these limitations, based on recent results (Kumar et al., 2022) for "indentation" problems akin to the one of interest in this work, we expect the choice of evolution Eq. (12) to provide useful insight. We will revisit the problem with a complete description of the strength of the solid in future work.

Remark. Under more general states of stress, the strength surface is more complicated due to the eigen decomposition of the strain in (10). A detailed description of how to construct the strength surface predicted by the original AT-1 model with such a spectral decomposition of the strain can be found in Appendix A of De Lorenzis and Maurini (2021). Fig. 3 illustrates the complete strength surface predicted by (12) in the general three-dimensional case and in plane stress ($\sigma_3 = 0$) using a tensile strength (σ_{ts}) of 20 MPa, for illustration. In plane stress conditions, the uniaxial tensile strength and the uniaxial compressive strength indicated by the strength surface are σ_{ts} and $\sigma_{cs} = \sqrt{(1+2\nu)(1-\nu)/2\nu^2}\,\sigma_{ts}$, respectively.

Note that the constitutive relation (10) satisfies automatically the balance of angular momentum (9). Substitution of the constitutive relation (10) in the balance of linear momentum (8) leads to

$$\text{div} \left[g(d)\frac{\partial \psi^+}{\partial \varepsilon}(\varepsilon(\boldsymbol{u})) + \frac{\partial \psi^-}{\partial \varepsilon}(\varepsilon(\boldsymbol{u})) \right] + \boldsymbol{b}_s = \rho_s \ddot{\boldsymbol{u}}, \quad (\boldsymbol{x},t) \in \Omega_s \times [0,T],$$

which together with the evolution Eq. (12) and appropriate initial and boundary conditions (to be spelled out next) for the displacement field $\boldsymbol{u}(\boldsymbol{x},t)$ and phase field $d(\boldsymbol{x},t)$ constitute the governing equations of elastodynamics and damage in the solid.

In the sequel, we shall consider that the solid is initially undeformed, at rest, stress free, that there is no initial damage, and that the body force is negligible:

$$\boldsymbol{u}(\boldsymbol{x},0) = \boldsymbol{0}, \; \dot{\boldsymbol{u}}(\boldsymbol{x},0) = \boldsymbol{0}, \; d(\boldsymbol{x},0) = 0, \quad \boldsymbol{x} \in \Omega_s,$$

and $\quad \boldsymbol{b}_s(\boldsymbol{x},t) = \boldsymbol{0}, \quad (\boldsymbol{x},t) \in \Omega_s \times [0,T].$

2.4. Fluid–solid interaction

The final step in the formulation of the problem is to describe the conditions at the fluid–solid interface Γ_{fs}. We assume a no-slip condition. Also, since the interest here is on hard brittle solids, we assume that surface tension effects are negligible. Precisely, we consider

$$\boldsymbol{u}|_s = \boldsymbol{u}|_f, \quad (\boldsymbol{x},t) \in \Gamma_{fs} \times [0,T], \tag{14}$$

and

$$\boldsymbol{\sigma}\boldsymbol{n}_s = -p\boldsymbol{n}_s, \quad (\boldsymbol{x},t) \in \Gamma_{fs} \times [0,T],$$

where $\boldsymbol{n}_s$ denotes the unit normal pointing outwards from the solid towards the fluid.

Noting that the acoustics problem in the fluid is fully described in terms of the pressure field p. By making use of relation (4), we can recast the jump condition (14) in terms of p as follows:

$$-\nabla p \cdot \boldsymbol{n}_s = \rho_f \ddot{\boldsymbol{u}}|_s \cdot \boldsymbol{n}_s, \quad (\boldsymbol{x},t) \in \Gamma_{fs} \times [0,T].$$
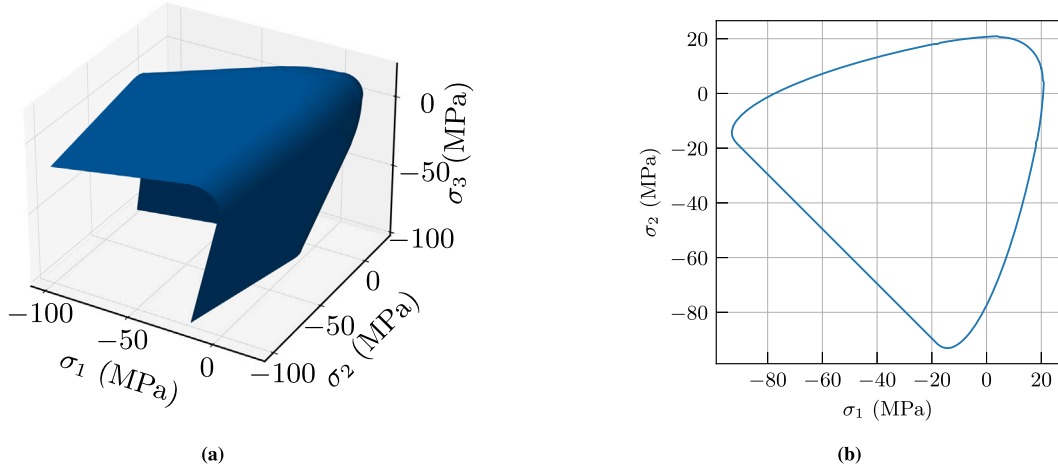
Fig. 3. Strength surface predicted by (12) for a material with a tensile strength of $\sigma_{ts} = 20$ MPa in (a) the principal stress space $(\sigma_1, \sigma_2, \sigma_3)$, and (b) plane stress states where $\sigma_3 = 0$.

Acoustics:	$\Delta p - \dfrac{1}{c_f^2} \ddot{p} = a,$		$(\boldsymbol{x}, t) \in \Omega_f \times [0, T]$
	$\nabla p \cdot \boldsymbol{n} = 0,$		$(\boldsymbol{x}, t) \in \Gamma_f \times [0, T]$
	$-\nabla p \cdot \boldsymbol{n}_s = \rho_f \ddot{\boldsymbol{u}} \cdot \boldsymbol{n}_s,$		$(\boldsymbol{x}, t) \in \Gamma_{fs} \times [0, T]$
	$p(\boldsymbol{x}, 0) = 0,$		$\boldsymbol{x} \in \Omega_f$
	$\dot{p}(\boldsymbol{x}, 0) = 0,$		$\boldsymbol{x} \in \Omega_f$
Elastodynamics:	$\text{div}\left[g(d) \dfrac{\partial \psi^+}{\partial \boldsymbol{\varepsilon}}(\boldsymbol{\varepsilon}(\boldsymbol{u})) + \dfrac{\partial \psi^-}{\partial \boldsymbol{\varepsilon}}(\boldsymbol{\varepsilon}(\boldsymbol{u})) \right] = \rho_s \ddot{\boldsymbol{u}},$		$(\boldsymbol{x}, t) \in \Omega_s \times [0, T]$
	$\left[g(d) \dfrac{\partial \psi^+}{\partial \boldsymbol{\varepsilon}}(\boldsymbol{\varepsilon}(\boldsymbol{u})) + \dfrac{\partial \psi^-}{\partial \boldsymbol{\varepsilon}}(\boldsymbol{\varepsilon}(\boldsymbol{u})) \right] \boldsymbol{n}_s = -p \boldsymbol{n}_s,$		$(\boldsymbol{x}, t) \in \Gamma_{fs} \times [0, T]$
	$\boldsymbol{u}(\boldsymbol{x}, 0) = \boldsymbol{0},$		$\boldsymbol{x} \in \Omega_s$
	$\dot{\boldsymbol{u}}(\boldsymbol{x}, 0) = \boldsymbol{0},$		$\boldsymbol{x} \in \Omega_s$
Damage:	$\text{div}\left[\ell \mathcal{G}_c \nabla d \right] = \dfrac{4}{3} g'(d) \psi^+(\boldsymbol{\varepsilon}(\boldsymbol{u})) + \dfrac{\mathcal{G}_c}{2\ell}, \quad \text{if } d(\boldsymbol{x}, t) > 0,$		$(\boldsymbol{x}, t) \in \Omega_s \times [0, T]$
	$\text{div}\left[\ell \mathcal{G}_c \nabla d \right] \leq \dfrac{4}{3} g'(d) \psi^+(\boldsymbol{\varepsilon}(\boldsymbol{u})) + \dfrac{\mathcal{G}_c}{2\ell}, \quad \text{if } d(\boldsymbol{x}, t) = 0,$		$(\boldsymbol{x}, t) \in \Omega_s \times [0, T]$
	$\nabla d \cdot \boldsymbol{n}_s = 0,$		$(\boldsymbol{x}, t) \in \Gamma_{fs} \times [0, T]$
	$d(\boldsymbol{x}, 0) = 0,$		$\boldsymbol{x} \in \Omega_s$

Box I.

We also assume that the initiation of damage is solely induced by the mechanical forces that result from the acoustic source. Accordingly, we consider a zero Neumann condition for the damage:

$$\nabla d \cdot \boldsymbol{n}_s = 0, \quad (\boldsymbol{x}, t) \in \Gamma_{fs} \times [0, T].$$

2.5. Governing equations

At this stage, we are in a position to combine the equations developed above into a mathematically closed system of governing equations for the pressure field $p(\boldsymbol{x}, t)$ in the fluid and the displacement field $u(\boldsymbol{x}, t)$ and phase field $d(\boldsymbol{x}, t)$ in the solid. They read

The strong form of the governing equations (see Box I)

3. Numerical implementation

In this section, we present a FE/FD scheme to approximate solutions for the governing equations of the coupled acoustics-eleastodynamics-damage problem derived above. We begin in Section 3.1 by recasting the strong form of the governing equations into a weak form. In Section 3.2, we then work out a Galerkin FE space discretization of the weak form. In Section 3.3, we further discretize in time the obtained set of space-discretized equations by means of FD. Finally, the scheme utilized to resolve the set of nonlinear algebraic equations resulting from the space and time discretizations is described in Section 3.4.

3.1. Weak form of the governing equations

For any fixed time $t \in [0, T]$, define the trial space $\mathcal{P}_t$ for the pressure field, $\mathcal{U}_t$ for the displacement field, and $\mathcal{D}_t$ for the damage field as

$$\mathcal{P}_t = \{ p(\boldsymbol{x}, t) \mid p(\boldsymbol{x}, t) \in \mathcal{H}^1(\Omega_f; \mathbb{R}) \},$$
$$\mathcal{U}_t = \{ \boldsymbol{u}(\boldsymbol{x}, t) \mid \boldsymbol{u}(\boldsymbol{x}, t) \in \mathcal{H}^1(\Omega_s; \mathbb{R}^N) \},$$
$$\mathcal{D}_t = \{ d(\boldsymbol{x}, t) \mid d(\boldsymbol{x}, t) \in \mathcal{H}^1(\Omega_s; \mathbb{R}), 0 \leq d \leq 1 \},$$

and the corresponding test spaces Q_t, V_t, and W_t as

$$Q_t = \{q(\boldsymbol{x}, t) \mid q(\boldsymbol{x}, t) \in \mathcal{H}^1(\Omega_f; \mathbb{R})\},$$
$$V_t = \{\boldsymbol{v}(\boldsymbol{x}, t) \mid \boldsymbol{v}(\boldsymbol{x}, t) \in \mathcal{H}^1(\Omega_s; \mathbb{R}^N)\},$$
$$W_t = \{w(\boldsymbol{x}, t) \mid w(\boldsymbol{x}, t) \in \mathcal{H}^1(\Omega_s; \mathbb{R})\}.$$

Define further $(\cdot, \cdot)$ as the inner product over the volume and $\langle \cdot, \cdot \rangle$ as the inner product over Neumann boundaries. A standard calculation shows that the weak form of the governing equations reads

The weak form of the governing equations

For $t \in [0, T]$, given $p(\boldsymbol{x}, 0) = 0$, $\dot{p}(\boldsymbol{x}, 0) = 0$, $\boldsymbol{u}(\boldsymbol{x}, 0) = 0$, $\dot{\boldsymbol{u}}(\boldsymbol{x}, 0) = 0$, and $d(\boldsymbol{x}, 0) = 0$, find $p(\boldsymbol{x}, t) \in \mathcal{P}_t$, $\boldsymbol{u}(\boldsymbol{x}, t) \in \mathcal{U}_t$, and $d(\boldsymbol{x}, t) \in \mathcal{D}_t$, such that $\forall q \in Q_t, \forall v \in \mathcal{V}$, and $\forall w \in W_t$,

$$\frac{1}{c_f^2}(\ddot{p}, q)_{\Omega_f} + (\nabla p, \nabla q)_{\Omega_f} + (a, q)_{\Omega_f} - \langle \rho_f q \ddot{\boldsymbol{u}}, \boldsymbol{n}_s \rangle_{\Gamma_{fs}} = 0, \quad (15a)$$

$$\rho_s (\ddot{\boldsymbol{u}}, \boldsymbol{v})_{\Omega_s} + (\boldsymbol{\sigma}, \nabla \boldsymbol{v})_{\Omega_s} + \langle p\boldsymbol{n}_s, \boldsymbol{v} \rangle_{\Gamma_{fs}} = 0, \quad (15b)$$

$$(\ell \mathcal{G}_c \nabla d, \nabla w)_{\Omega_s} + \left(\frac{4}{3}g'(d)\psi_e^+(\varepsilon(\boldsymbol{u})) + \frac{\mathcal{G}_c}{2\ell}, w\right)_{\Omega_s} \geq 0. \quad (15c)$$

3.2. Space discretization

Consider now a conforming partition of the domain $\Omega = \Omega_f \cup \Omega_s$ occupied by the fluid and the solid in their initial configuration into non-overlapping simplicial finite elements $\{\Omega^e\}_{e=1}^{n_{el}}$; a typical partition is illustrated in Fig. 10, where a mesh of linear triangular elements is used in both the solid and fluid domains. Given this partition, in the finite-element space consisting of continuous piecewise linear polynomial functions, we look for approximations $p_h(\boldsymbol{x}, t)$ of the pressure field $p(\boldsymbol{x}, t)$ in the fluid domain, and $\boldsymbol{u}_h(\boldsymbol{x}, t)$ and $d_h(\boldsymbol{x}, t)$ of the displacement field $\boldsymbol{u}(\boldsymbol{x}, t)$ and the phase field $d(\boldsymbol{x}, t)$ in the solid domain. We denote these spaces by $\mathcal{P}_t^h \subset \mathcal{P}$, $\mathcal{U}_t^h \subset \mathcal{U}_t$, and $\mathcal{D}_t^h \subset \mathcal{D}_t$. We make use of a standard Galerkin approximation and denote the corresponding test subspaces by $Q_t^h \subset Q_t$, $\mathcal{V}_t^h \subset \mathcal{V}_t$, and $W_t^h \subset W_t$. In this setting, it is trivial to deduce that the spatial discretization of the weak form (15) is given by:

The Galerkin FE form of the governing equations

For $t \in [0, T]$, given $p_h(\boldsymbol{x}, 0) = 0$, $\dot{p}_h(\boldsymbol{x}, 0) = 0$, $\boldsymbol{u}_h(\boldsymbol{x}, 0) = 0$, $\dot{\boldsymbol{u}}_h(\boldsymbol{x}, 0) = 0$, $d_h(\boldsymbol{x}, 0) = 0$, find $p_h(\boldsymbol{x}, t) \in \mathcal{P}_t^h$, $\boldsymbol{u}_h(\boldsymbol{x}, t) \in \mathcal{U}_t^h$, and $d_h(\boldsymbol{x}, t) \in \mathcal{D}_t^h$, such that $\forall q_h \in Q_t^h, \forall v_h \in \mathcal{V}_t^h$, and $\forall w_h \in W_t^h$,

$$\frac{1}{c_f^2}(\ddot{p}_h, q_h)_{\Omega_f} + (\nabla p_h, \nabla q_h)_{\Omega_f} + (a, q_h)_{\Omega_f} - \langle \rho_f q_h \ddot{\boldsymbol{u}}_h, \boldsymbol{n}_s \rangle_{\Gamma_{fs}} = 0, \quad (16a)$$

$$\rho_s (\ddot{\boldsymbol{u}}_h, \boldsymbol{v}_h)_{\Omega_s} + (\boldsymbol{\sigma}_h, \nabla \boldsymbol{v}_h)_{\Omega_s} + \langle p_h \boldsymbol{n}_s, \boldsymbol{v}_h \rangle_{\Gamma_{fs}} = 0, \quad (16b)$$

$$(\ell \mathcal{G}_c \nabla d_h, \nabla w_h)_{\Omega_s} + \left(\frac{4}{3}g'(d_h)\psi_e^+(\varepsilon(\boldsymbol{u}_h)) + \frac{\mathcal{G}_c}{2\ell}, w_h\right)_{\Omega_s} \geq 0, \quad (16c)$$

where we remark that the space-discretized inequality (16c) for the damage evolution associated with the irreversibility constraint $\dot{d}_h \geq 0$ is treated with a Primal–Dual Active Set (PDAS) strategy (Heister et al., 2015).

It follows that Eqs. (16) reduce to a system of ordinary differential equations and nonlinear algebraic (in)equalities for the resulting global degrees of freedom, say, in vector form, $\mathbf{p}(t)$, $\mathbf{u}(t)$, and $\mathbf{d}(t)$, of the matrix form

$$\begin{cases} \boldsymbol{M}_f \ddot{\mathbf{p}}(t) + \boldsymbol{K}_f \mathbf{p}(t) = \boldsymbol{F}_f(t, \ddot{\mathbf{u}}(t)), \quad t \in [0, T] \\ \mathbf{p}(0) = \mathbf{0}, \\ \dot{\mathbf{p}}(0) = \mathbf{0}, \end{cases} \quad (17)$$

for the pressure field p_h in the fluid,

$$\begin{cases} \boldsymbol{M}_s \ddot{\mathbf{u}}(t) + \boldsymbol{G}_s(\mathbf{u}(t), \mathbf{d}(t)) = \boldsymbol{F}_s(\mathbf{p}(t)), \quad t \in [0, T] \\ \mathbf{u}(0) = \mathbf{0}, \\ \dot{\mathbf{u}}(0) = \mathbf{0}, \end{cases} \quad (18)$$

for the displacement field $\boldsymbol{u}_h$ in the solid, and

$$\begin{cases} \boldsymbol{R}_s(\mathbf{u}(t), \mathbf{d}(t)) \geq \mathbf{0}, \quad t \in [0, T] \\ \dot{\mathbf{d}}(t) \geq \mathbf{0}, \quad t \in [0, T] \\ \mathbf{d}(0) = \mathbf{0}, \end{cases} \quad (19)$$

for the phase field d_h in the solid.

In Eqs. (17), $\boldsymbol{M}_f$, $\boldsymbol{K}_f$, and $\boldsymbol{F}_f$ denote, respectively, the constant mass matrix, the constant stiffness matrix, and the forcing vector in the fluid domain. As indicated by its arguments, note that the forcing vector $\boldsymbol{F}_f$ is *not* a constant but a function of time, via its dependence on the acoustic point source, and of the acceleration of the solid at the fluid–solid interface.

In Eqs. (18), $\boldsymbol{M}_s$ denotes the constant mass matrix in the solid domain, while the vectors $\boldsymbol{G}_s$ and $\boldsymbol{F}_s$ are functions of the degrees of freedom of the displacement field and the phase field and of the pressure field, as indicated by their arguments.

Finally, in the (in)equalities (19), the vector $\boldsymbol{R}_s$ is a nonlinear function of the degrees of freedom of the displacement field and the phase field in the solid domain and the short notation $\dot{\mathbf{d}}(t) \geq \mathbf{0}$ is employed to denote that each of the components of the vector $\dot{\mathbf{d}}(t)$ is constrained to be nonnegative.

3.3. Time discretization

Consider next a partition of the time interval under consideration $[0, T]$ in the space-discretized Eqs. (17)–(19) into discrete times $0 = t_0, t_1, \ldots t_m, t_{m+1}, \ldots, t_M = T$. Making use of the notation $\mathbf{p}_m = \mathbf{p}(t_m)$, $\mathbf{u}_m = \mathbf{u}(t_m)$, $\mathbf{d}_m = \mathbf{d}(t_m)$ for $m = 0, 1, \ldots, M-1, M$, $\Delta t_m = t_{m+1} - t_m$, and the second-order central difference approximation for the time derivatives

$$\ddot{\mathbf{p}}(t_m) = \frac{\mathbf{p}_{m+1} - 2\mathbf{p}_m + \mathbf{p}_{m-1}}{(\Delta t_m)^2} \quad \text{and} \quad \ddot{\mathbf{u}}(t_m) = \frac{\mathbf{u}_{m+1} - 2\mathbf{u}_m + \mathbf{u}_{m-1}}{(\Delta t_m)^2}, \quad (20)$$

it follows that the solution $\mathbf{p}_{m+1}$, $\mathbf{u}_{m+1}$, $\mathbf{d}_{m+1}$ of the Eqs. (17)–(19) at the discrete time t_{m+1} is given in terms of the solution at the previous times by the system of coupled nonlinear algebraic equations

$$\begin{cases} \boldsymbol{M}_f \dfrac{\mathbf{p}_{m+1} - 2\mathbf{p}_m + \mathbf{p}_{m-1}}{(\Delta t_m)^2} + \boldsymbol{K}_f \mathbf{p}_m \\ = \boldsymbol{F}_f \left(t_m, \dfrac{\mathbf{u}_{m+1} - 2\mathbf{u}_m + \mathbf{u}_{m-1}}{(\Delta t_m)^2} \right) \\ \boldsymbol{M}_s \dfrac{\mathbf{u}_{m+1} - 2\mathbf{u}_m + \mathbf{u}_{m-1}}{(\Delta t_m)^2} + \boldsymbol{G}_s(\mathbf{u}_m, \mathbf{d}_m) = \boldsymbol{F}_s(\mathbf{p}_m) \\ \begin{cases} \boldsymbol{R}_s(\mathbf{u}_{m+1}, \mathbf{d}_{m+1}) \geq \mathbf{0} \\ \mathbf{d}_{m+1} - \mathbf{d}_m \geq \mathbf{0} \end{cases} \end{cases} \quad m = 0, 1, \ldots, M-1, M. \quad (21)$$

Initial conditions. To implement the initial conditions in $(21)_{1,2}$, we make use of a ghost grid point at $t_{m=-1}$ together with the first-order approximations

$$\mathbf{p}_{-1} = \mathbf{p}_1 - 2\Delta t_0 \dot{\mathbf{p}}(0) = \mathbf{p}_1 \quad \text{and} \quad \mathbf{u}_{-1} = \mathbf{u}_1 - 2\Delta t_0 \dot{\mathbf{u}}(0) = \mathbf{u}_1$$

in terms of the initial conditions for $\dot{\mathbf{p}}(t)$ and $\dot{\mathbf{u}}(t)$ at $t = 0$.

In all the simulations presented in Section 5 below, we make use of a uniform time increment $\Delta t_m = \Delta t$ that is selected so as to satisfy the CFL (Courant–Friedrichs–Levy) condition in both the fluid and the solid domains (Courant et al., 1928). Precisely, we set

$$\Delta t \leq \min \left\{ \frac{h_f}{c_f}, \frac{h_s}{c_s} \right\},$$

where h_f and h_s stand for the sizes of the smallest elements in the fluid and the solid, $c_f = \sqrt{K_f / \rho_f}$, and $c_s = \sqrt{(2\mu + \lambda) / \rho_s}$.
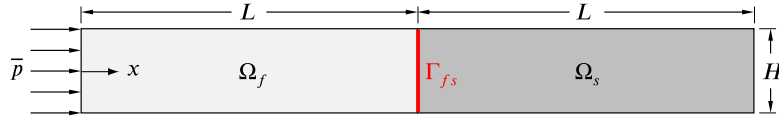
Fig. 4. Schematic of the acoustics-elastodynamics-damage benchmark problem. A pressure is applied at the left boundary of a fluid domain, which is connected to a solid domain of the same dimensions, $L \times H$.

Table 1
Baseline material properties for the fluid and the solid used in the NPL simulations.

Property	Symbol	Unit	Value
Mass density of the fluid	ρ_f	g/mm³	1×10^{-3}
Mass density of the solid	ρ_s	g/mm³	1.995×10^{-3}
Wave speed in the fluid	c_f	mm/µs	1.5
P wave speed in the solid	c_s	mm/µs	4.159
Leaky Rayleigh wave speed	c_{LRW}	mm/µs	2.141
Young's modulus	E	MPa	2.735×10^4
Poisson's ratio	ν	/	0.2
Critical energy release rate	G_c	N/mm	2.188×10^{-2}
Uniaxial tensile strength	σ_{ts}	MPa	20
Nucleation energy	ψ_c	MPa	7×10^{-3}

3.4. Solver

The choice of second-order central difference approximations (20) for the second time derivatives of the pressure and the displacement fields leads to a system of discretized Eqs. (21) that is *one-way coupled* and hence, as outlined next, can be solved sequentially at every discrete time without any iteration between the solves of (21)₁, (21)₂, and (21)₃.

Consider that the solutions $\mathbf{p}_n$, $\mathbf{u}_n$, $\mathbf{d}_n$ ($n = 0, 1, \ldots, m-1, m$) of the Eqs. (17)–(19) up to the discrete time t_m have been determined. Then

1. Eq. (21)₁ can be solved for $\mathbf{p}_{m+1}$.
2. Having determined $\mathbf{p}_{m+1}$, Eq. (21)₂ can then be solved for $\mathbf{u}_{m+1}$.
3. Having determined $\mathbf{p}_{m+1}$ and $\mathbf{u}_{m+1}$, Eq. (21)₃ can in turn be solved for $\mathbf{d}_{m+1}$.

Having computed $\mathbf{p}_{m+1}$, $\mathbf{u}_{m+1}$, $\mathbf{d}_{m+1}$ in this manner, one can move on to compute the solution at the next discrete time t_{m+2}.

The above-outlined scheme to generate numerical solutions for the acoustics-elastodynamics-damage problem formulated in the preceding section was implemented in RACCOON, a massively parallel FE code built upon the MOOSE framework (Permann et al., 2020) maintained by Idaho National laboratory. All the simulations presented next were generated with that implementation.

4. A benchmark problem

In the sequel, we deploy the numerical scheme presented above to simulate various acoustics-elastodynamics-damage problems. We begin with a simple benchmark problem that serves to verify the implementation of the scheme.

Consider the problem in $N = 2$ space dimensions schematically depicted in Fig. 4, wherein the source term $a = 0$ but a pressure is applied at the left boundary $(x_1 = 0, x_2)$ of a fluid domain of dimensions $L \times H$, so that an acoustic wave propagates through the fluid and eventually reaches a solid domain also of dimensions $L \times H$. The right boundary $(x_1 = 2L, x_2)$ of the solid domain is traction free.

The fluid and the solid are assumed to be characterized by the material properties listed in Table 1, save for the Poisson's ratio, which is set to $\nu = 0$ here.

Specifically, the applied pressure is given by

$$p(0, x_2, t) = \begin{cases} A \sin(4\pi t) & \text{if } t \le t_p \\ 0 & \text{else } t > t_p, \end{cases}$$

where the amplitude of the pulse is chosen to match roughly half of the uniaxial tensile strength of the material, $2A/\sigma_{ts} = 1.1$, while the
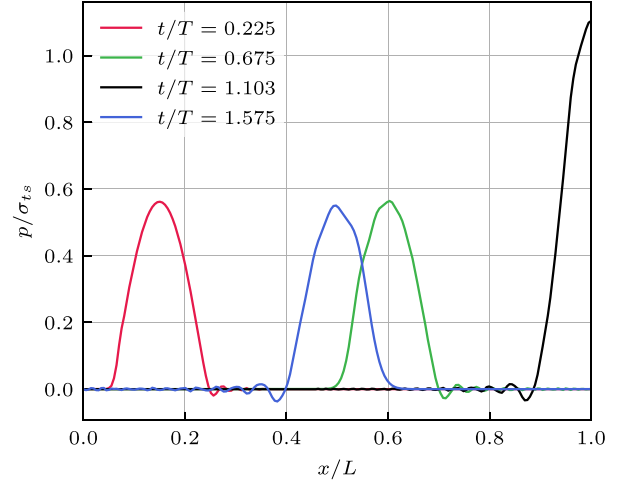

Fig. 5. Temporal variation of the normalized pressure p/σ_{ts} in the fluid domain.

time period t_p is set to correspond to the time required for the pulse to propagate over roughly 20% of the length of the fluid domain, that is, $t_p/T = 0.1875$, where $T = L/c_f$.

To carry out the simulations, we discretized the domain with a uniform FE mesh of element size $h = L/200$ and made use of the time step $\Delta t = 0.2h/c_s$.

Although the problem is simulated in $N = 2$ space dimensions, due to the material properties and initial and boundary conditions, none of the fields vary in the thickness (x_2) direction. As such, the problem is essentially one-dimensional. We therefore write $x_1 = x$.

Fig. 5 shows the acoustic wave in the fluid domain at several snapshots in time. The wave can be seen to begin at the left boundary, propagate to the right, and then reflect back at the fluid–solid interface. As the solid domain is far stiffer than the fluid domain, the reflected wave in the fluid domain has only a slightly smaller amplitude than the incoming wave.

The component of the normalized stress σ_{11}/σ_{ts} in the solid domain is plotted in Fig. 6 for two different time periods. Fig. 6(a) shows snapshots of the compressive stress that develops in the solid at times $1.125 \le t/T < 1.388$. As the wave impacts the right boundary of the solid domain, it reflects off the free surface and becomes tensile. The normalized tensile stress that develops for times $1.5 \le t/T < 1.575$ is shown in Fig. 6(b). The peak of the tensile wave is sufficiently large such that the "tensile" strain energy ψ^+ exceeds the nucleation energy ψ_c and damage develops.

Plots of the normalized "tensile" strain energy and the damage at time $t/T = 1.575$ are shown in Fig. 7. The damage that develops is relatively small in magnitude, but this is consistent with the peak strain energy being only slightly larger than the threshold for damage to develop.

Although an analytical solution is not available for this problem, qualitatively, the results are consistent with expectations. From the results shown in Figs. 5 and 6, one can also evaluate the discrete wave speeds in both the fluid and solid domains. Compared to the wave speeds c_f and c_s listed in Table 1, the simulated fluid and solid wave speeds were found to have errors smaller than 4%. Finally, to
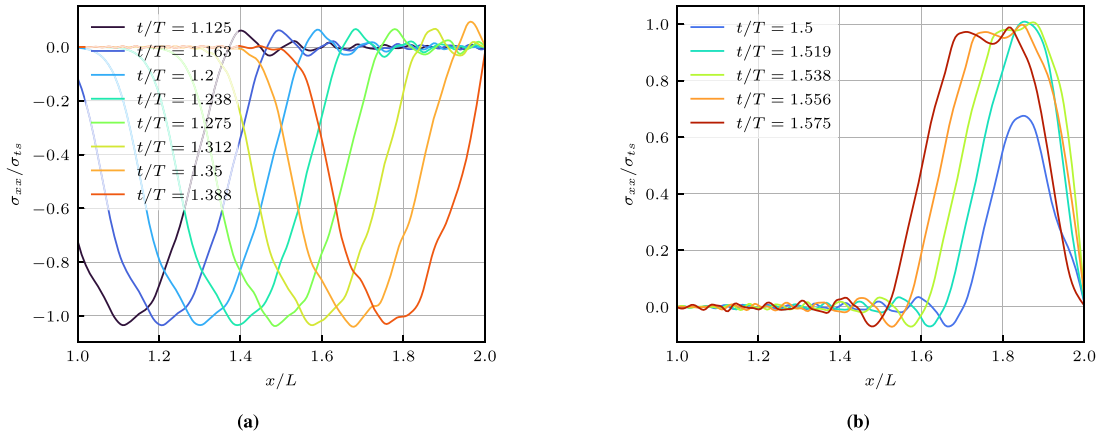
Fig. 6. Temporal variation of the normalized stress σ_{11}/σ_{ts} in the solid domain (a) before the compressive wave reaches the right boundary, and (b) after the wave reflects off the right boundary and becomes tensile.
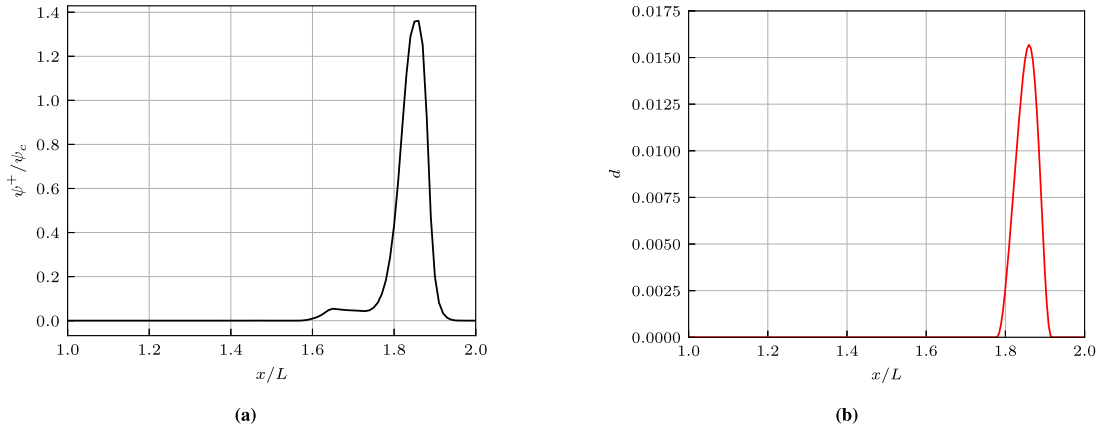

Fig. 7. Variation of (a) the normalized "tensile" strain energy ψ^+/ψ_c and (b) the damage d in solid the domain at $t/T = 1.575$.

demonstrate spatial convergence in the damage field, the calculation is repeated over a sequence of increasingly refined meshes with uniform mesh spacing $h \in [L/50, L/100, L/200]$ (with the time step scaled as $\Delta t = 0.2 h/c_s$). The results in the solid domain at time $t/T = 1.575$ are shown in Fig. 8. The results for the two finest discretizations are practically indistinguishable.

5. NPL simulations

We now turn to the simulations of primary interest in this work, to wit, model-based simulations of NPL experiments. We begin by describing the setup used to examine these experiments and the results of representative simulations. We then perform a parameter study that examines how damage develops as a function of the strength and the proximity of the acoustic source to the solid surface as well as of the fracture resistance of the solid. Finally, we explore possible reasons that may explain some of the differences between the simulation results and the experimental observations.

5.1. The geometry of the problem and its FE discretization

Fig. 9 depicts schematically the NPL experiment of interest here. The problem consists of a solid, occupying the cylindrical domain $\Omega_s = \{\boldsymbol{x} : \sqrt{x_1^2 + x_2^2} < R, \, 0 < x_3 < H\}$, that is immersed near the bottom of a fluid domain, occupying the larger cylindrical domain $\Omega_f = \Omega \setminus \Omega_s$ with $\Omega = \{\boldsymbol{x} : \sqrt{x_1^2 + x_2^2} < 1.1R, \, -H/3 < x_3 < 3H\}$, wherein there is an acoustic point source located at a standoff distance S_d with respect to the surface of the solid along its axis of symmetry. The values of
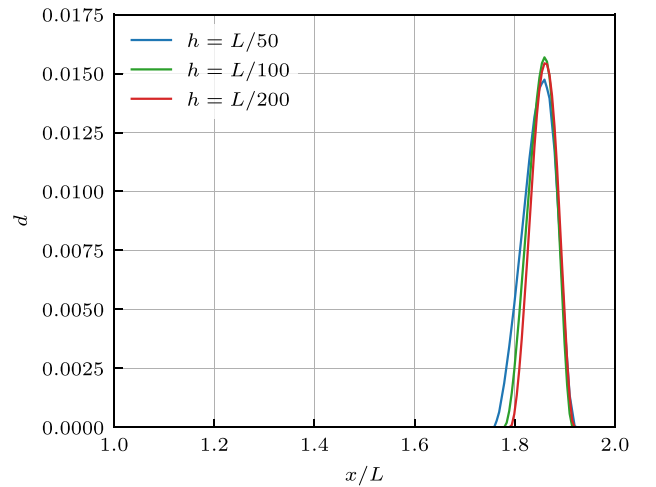

Fig. 8. Comparison of the damage profile in the solid domain at $t/T = 1.575$ over a sequence of refined meshes with mesh spacing $h \in [L/50, L/100, L/200]$ and time steps $\Delta t = 0.2 h/c_s$.

the radius R and the height H of the solid domain and of the range of standoff distances S_d used in the simulations are listed in Table 2.

Because of the symmetry of the geometry of the fluid and solid bodies, their isotropic material properties (spelled out below), and
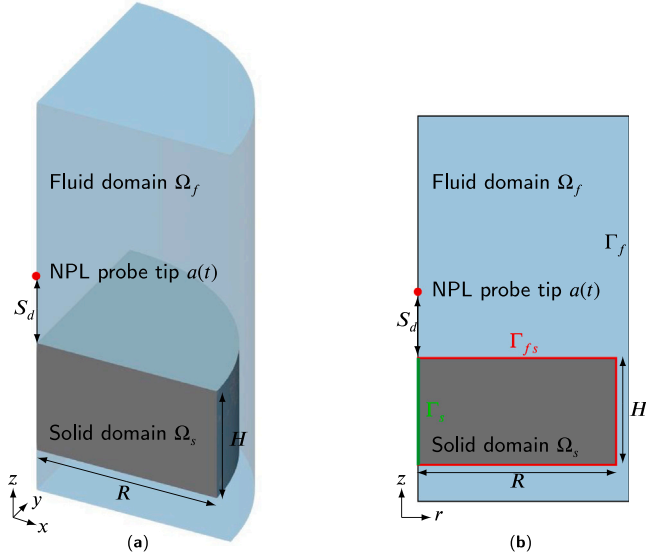
Fig. 9. Schematic of the NPL experiment (a) from a three-dimensional perspective and (b) from the corresponding axisymmetric perspective.

Table 2
Parameters for the geometry of the solid domain and the range of locations of the acoustic point source used in the NPL simulations.

Parameter	Symbol	Unit	Value
Radius of the solid domain	R	mm	3.25
Height of solid domain	H	mm	2
Standoff distance	S_d	mm	[0.25, 1.5]

the symmetry of the applied loading, the problem features axisymmetric symmetry and therefore can be treated mathematically as a two-dimensional problem. Fig. 9(b) shows the two-dimensional domain considered from this axisymmetric perspective.

Fig. 10 shows a representative FE mesh used to carry out the axisymmetric simulations of the NPL experiment. As shown by Fig. 10(b), the mesh is conforming and fitted to both domains so as to facilitate the enforcement of the transmission conditions at the fluid–solid interface Γ_{fs}.

5.2. Loading, material, and computational parameters

The values of the parameters describing the acoustic point source and the baseline material properties used for the simulations are listed in Table 3 and Table 1, respectively.

The acoustic point source, is prescribed according to

$$a(\mathbf{x}, t) = \frac{4\pi}{\rho_f} S_0(t)\delta(\mathbf{x} - \mathbf{x}_s), \tag{22}$$

where

$$S_0(t) = \frac{c_1}{c_2} p_0 d_1 \left\langle \left(1 + \tanh \frac{t - t_1}{t_R} \right) \exp{-\frac{t - t_1}{t_L}} \cos\left(2\pi f_L(t - t_1) + \frac{\pi}{3} \right) \right\rangle_+. \tag{23}$$

The magnitude and temporal signal for this source correspond to a typical lithotripsy pulse, albeit one that is modified with a hyperbolic tangent function to provide a smooth sharp wavefront (Cleveland and Sapozhnikov, 2005). In this work, a volume source with radius r_0 ($r_0 \ll R$) is adopted to approximate the Dirac delta in (22), so that,

$$\int_\Omega \delta(\mathbf{x} - \mathbf{x}_s) S_0(t) \, \mathrm{d}\mathbf{x} \approx \int_{B_{r_0}} C_v S_0(t) \, \mathrm{d}\mathbf{x}, \tag{24}$$

where B_{r_0} denotes a small ball centered at $\mathbf{x}_s$, with radius $r = r_0$.

The point source gives rise to a pressure pulse in the axisymmetric acoustic domain that is shown as a function of time in Fig. 11. The results are shown in terms of the normalized time $\bar{t} = t/T$, where $T = 2$ μs is the characteristic time. Roughly speaking, the characteristic time corresponds to approximately twice the duration of the acoustic source. The magnitude of the pressure source and its temporal signal were chosen to match the experimental measurements provided in Yang (2018).

The material properties listed in Table 1 for the solid were chosen to be consistent with those of 'BegoStone' (Liu and Zhong, 2002), a synthetic material often used as a "phantom" for kidney stones in laboratory experiments. The material properties listed in Table 1 for the fluid are consistent with those of water.

Finally, we note that all the simulations were carried out with a value of $\ell = 0.1$ mm for the regularization length and a uniform time step $\Delta t = 7.5 \times 10^{-4}$ μs.

5.3. Spherical wave interaction at the fluid–solid boundary

In a simulation of a single pulse from a NPL device, a spherical acoustic wave is initiated from the point source and propagates in the fluid. The acoustic wave eventually interacts with the solid through transmission at the fluid–solid interface. This type of acoustic-solid interaction has been studied in detail by de Hoop and van der Hijden (1984) and more recently by Zhang et al. (2017).

To illustrate the response in both the fluid and solid domains, we begin by considering the case where the standoff distance is $S_d/R = 0.23$. Fig. 12 provides contour plots of the normalized pressure p/σ_{ts} in the fluid domain and the normalized "tensile" strain energy ψ^+/ψ_c in the solid domain at various points in time. The results are shown in terms of the normalized time $\bar{t} = t/T$, where, again, $T = 2$ μs is the characteristic time.

At early times, the spherical pressure wave propagates in the fluid domain while the solid domain remains undisturbed. Then the pressure wave reaches the solid interface and reflects off the surface. The fluid–solid interaction gives rise to a surface acoustic wave – commonly referred to as a leaky Rayleigh wave – in the solid that propagates at a speed of c_{LRW}.

At later times, as shown by Fig. 12(c), the simulation results clearly indicate the separate longitudinal and transverse branches of the leaky Rayleigh wave. The surface wave propagates from the center of the top surface towards the outer edge of the domain, and the position of the peak value of the strain energy also moves from the surface center to the right end of the solid domain.

In this study, we consider a single pulse simulation to consist of the time required for the acoustic source to fully subside. Consistent with Fig. 11, this corresponds to $\bar{t} \in [0, 1.0]$. We note that at $\bar{t} = 1.0$, the pressure wave in the fluid domain will have just reached the right side of the fluid boundary. This final time is also sufficient for the "tensile" strain energy on the surface of the solid domain to have reached a peak and for the leaky Rayleigh wave to have reached the edge of the solid domain.

We now examine the pressure, the stress, and the strain energy at the top surface of the solid domain. In Fig. 13, we plot the normalized "tensile" strain energy, stress, and the transferred pressure on the top surface of the solid at $\bar{t} = 0.675$. Fig. 13(b) shows that the transferred pressure matches the axial stress component σ_{zz}. Fig. 14 shows the temporal variation in the normalized radial stress and the "tensile" strain energy on the top surface over the time interval $\bar{t} \in [0, 1.0]$. These plots illustrate how the tensile stress wave and "tensile" strain energy gradually increase in time and reach a peak at some distance before $r/R = 1.0$. This effect is critical in governing the evolution of the damage on the surface.

Similar results and observations have been reported by Zhang et al. (2019) for model-based simulations (using COMSOL) of nanosecond acoustic wave induced surface acoustic waves. In particular, their

Table 3

Parameters in the strength (23) and regularization (24) of the acoustic point source used in the NPL simulations.

Parameter	c_1	c_2	d_1	t_1	t_R	t_L	f_L	p_0	C_v	r_0
Unit	/	/	mm	μs	μs	μs	μs^{-1}	MPa	mm^{-1}	mm
Value	12.2189	0.9404	9	0.07	0.01	0.8	0.0833	2.1×10^{-2}	1000	0.1
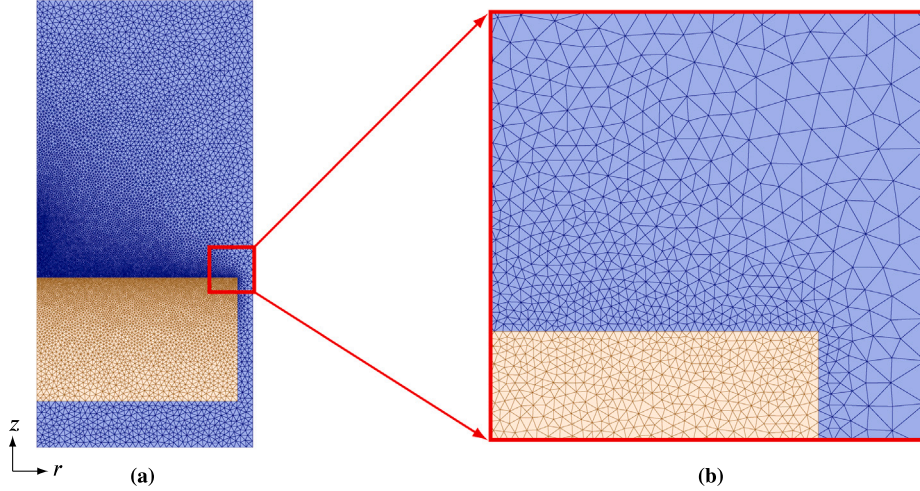
Fig. 10. A representative axisymmetric FE mesh used for the NPL simulations. (b) An enlarged view of the boundary between the solid and fluid domains.
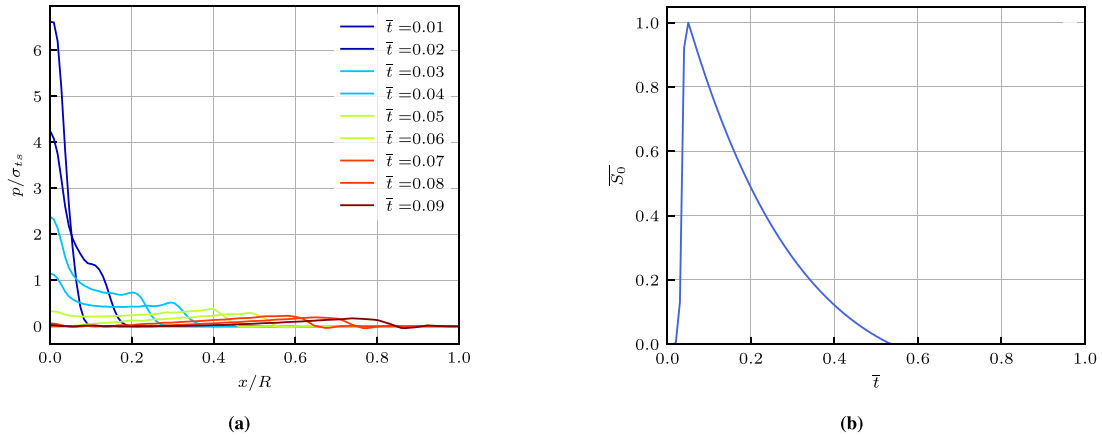
Fig. 11. (a) Variation of the effective acoustic strength $\overline{S_0} = C_v S_0/\sigma_{ts}$ in time. (b) The resulting normalized pressure p/σ_{ts} as a function of distance from the point source during $\bar{t} \in [0.01, 0.09]$.

simulation results of an NPL-induced acoustic wave interaction at a water-glass boundary indicated that the first principal stress along the top surface of the solid domain exhibited a similar profile to our results shown in Fig. 14(a).

5.4. Parametric study

We now provide a parametric study in which the sensitivity of the simulated damage profile to variations in select model parameters is examined. In particular, we examine how variations in the driving forces (standoff distance, pressure magnitude) and the material properties governing the fracture resistance of the solid impact the resulting damage profile.

5.4.1. Influence of standoff distance S_d and acoustic source strength

We begin by varying the standoff distance, while keeping all other parameters fixed. Recall that in the cohesive-type phase-field model

that we are employing here to describe damage, the nucleation energy ψ_c is the parameter that mostly controls the nucleation of damage. In particular, damage is expected to develop in regions within the solid where $\psi^+ > \psi_c$.

Fig. 15 presents plots of the maximum value of the normalized "tensile" strain energy $\psi^+ > \psi_c$ and the associated damage profiles along the surface of the solid for six different standoff distances. As the standoff distance increases, the damaged region moves outward from the center of the domain, and decreases in magnitude. The latter behavior corresponds to the strength of the pressure wave that impacts the solid being smaller as the point source is moved further from the surface. The rightward shift of the damaged region corresponds to the nonlinear interaction between the incoming (compressive) pressure wave and the reflected pressure wave being delayed in time as the standoff distance increases. In essence, it takes a longer time for the surface acoustic wave on the solid surface to result in a "tensile" strain energy that exceeds ψ_c.
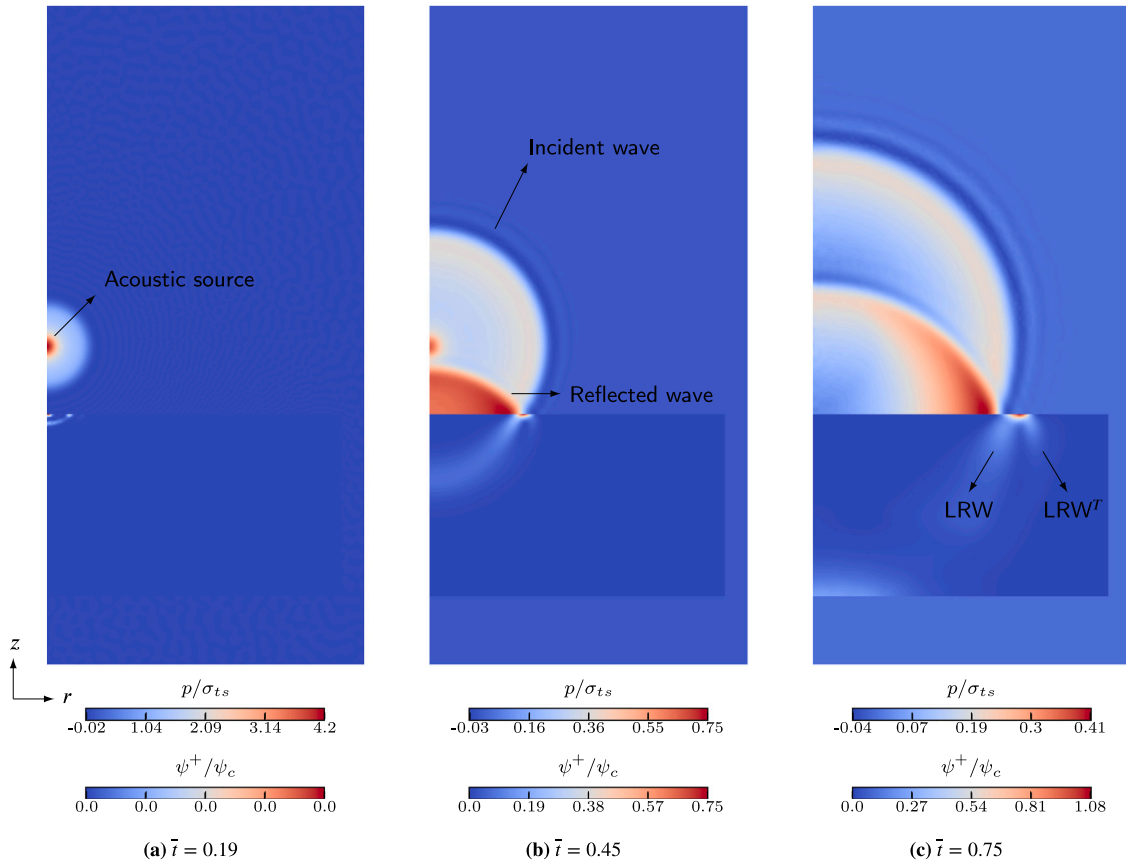
Fig. 12. Contour plots of the normalized pressure p/σ_{ts} in the fluid domain and normalized "tensile" strain energy ψ^+/ψ_c in the solid domain for $S_d/R = 0.23$ at three time instances: (a) at $\bar{t} = 0.19$ before the incident wave reaches the solid domain, (b) at $\bar{t} = 0.45$ after the incident wave hits the solid and is reflected from its boundary, and (c) at $\bar{t} = 0.75$ when the incident and reflected waves further propagate in the fluid domain. LRW and LRW^T illustrate the longitudinal and transverse branches of the leaky Rayleigh wave.
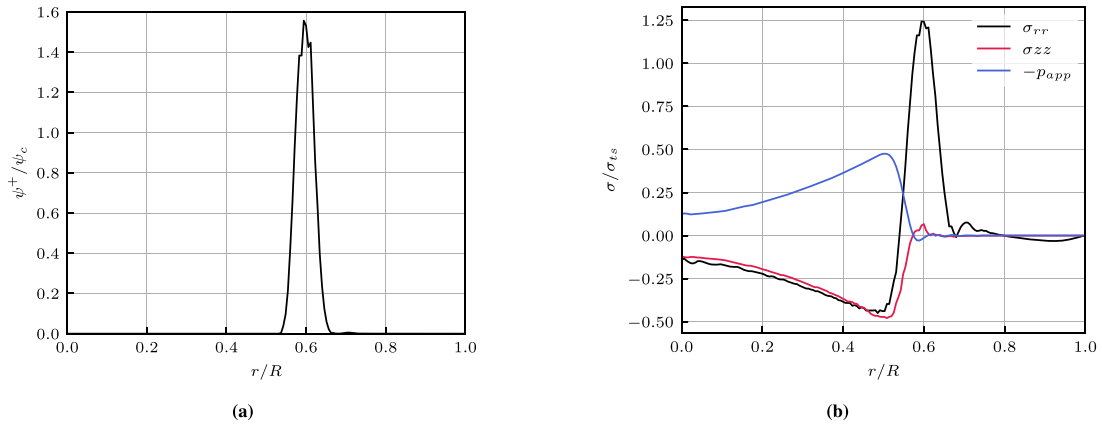
Fig. 13. Variation of (a) the normalized "tensile" strain energy ψ^+/ψ_c and (b) the normalized radial stress σ_{rr}/σ_{ts}, transferred pressure $-p_a/\sigma_{ts}$ from the fluid to the solid domain, and the axial stress component σ_{zz}/σ_{ts} on the top surface of the solid. The results pertain to the case of $S_d/R = 0.23$ at $\bar{t} = 0.675$, corresponding to the contours presented in Fig. 12.

The damage field is illustrated in another manner in Fig. 16. In particular, Fig. 16(a) illustrates how the size of the damaged region decreases as the standoff distance is increased. At some point, the standoff distance is so large that almost no damage develops on the surface, as shown in Fig. 16(b). Importantly, both of these trends qualitatively match experimental observations of damage patterns on the surface of materials subjected to nano-pulse acoustic waves, as reported by Yang (2018) and Zhang et al. (2019).

We now examine how variations in the strength of the acoustic source impact the simulated damage fields, for several standoff distances. To report the results, we indicate the magnitude of the pressure relative to the base value p_0 provided in Table 3 by $\overline{p_0}$. So a value of $\overline{p_0} = 2.0$ represents an acoustic pressure source that is twice as large as the base value. We examine the sensitivity of the damage in response to a range of acoustic sources of varying strengths corresponding to $\overline{p_0} \in [0.6, 3.0]$.
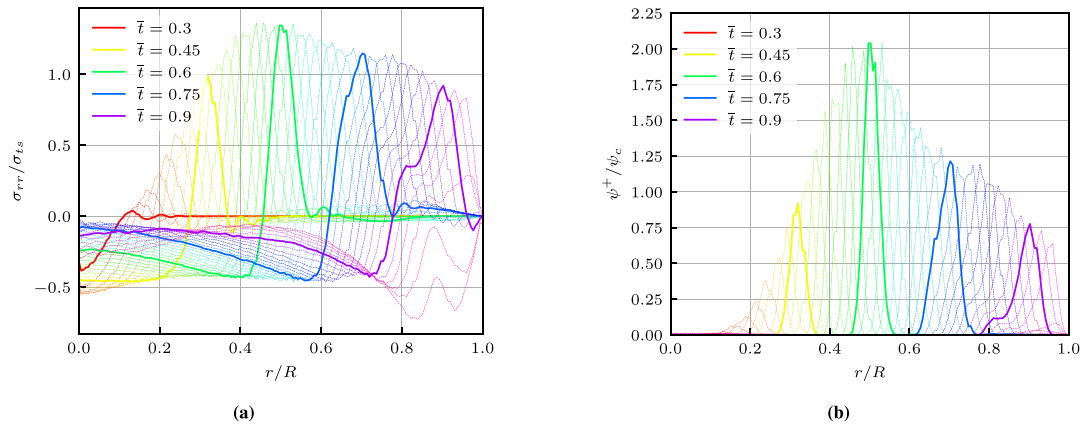
Fig. 14. Temporal variation of (a) the normalized radial stress σ_{rr}/σ_{ts} and (b) the normalized "tensile" strain energy ψ^+/ψ_c on the top surface of the solid domain. The results pertain to the case $S_d/R = 0.23$.
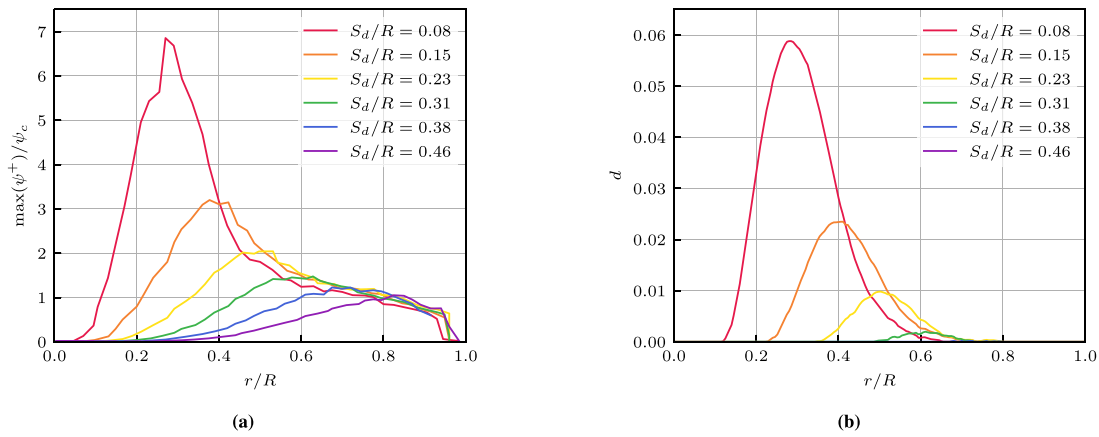

Fig. 15. Variation of (a) the maximum normalized "tensile" strain energy $\max\{\psi^+/\psi_c\}$ and (b) the damage d for six different standoff distances $S_d/R = 0.08, 0.15, 0.23, 0.31, 0.38, 0.46$ on the top surface of the solid.
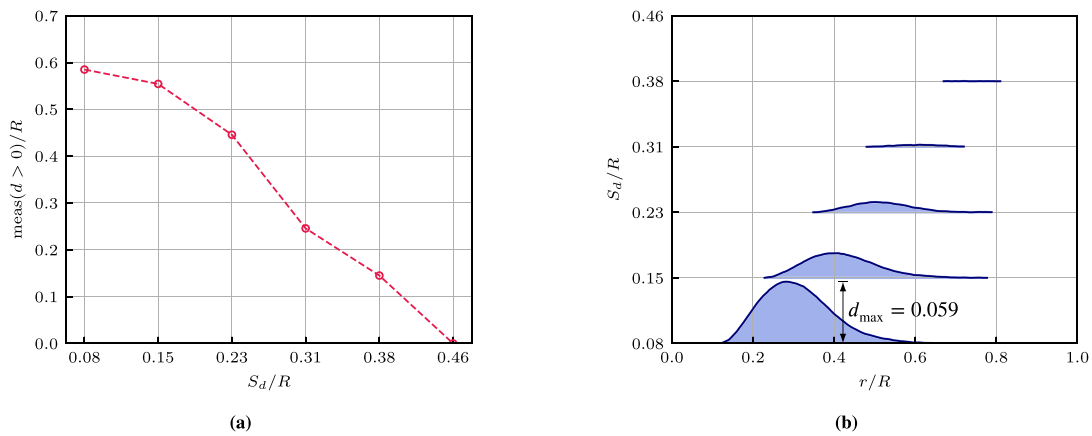

Fig. 16. Visualization of the damaged region on the surface of the solid. (a) Measures of the damaged region $d > 0$. (b) The stack plots for the range of the damage region and qualitative damage magnitude at six different standoff distances $S_d/R = 0.08, 0.15, 0.23, 0.31, 0.38, 0.46$ on the top surface of the solid.
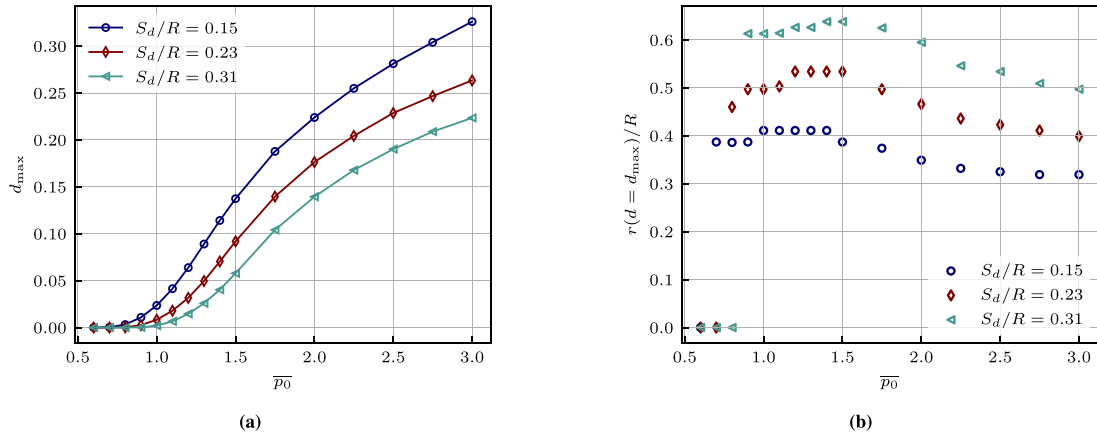
(a)

(b)

Fig. 17. Sensitivity of the damage field on the surface of the solid domain in response to variations in the acoustic source strength p_0. (a) Maximum damage d_{max} as a function of $\overline{p_0}$. (b) Radial position of the maximum damage $r|_{d=d_{max}}/R$ as a function of $\overline{p_0}$.
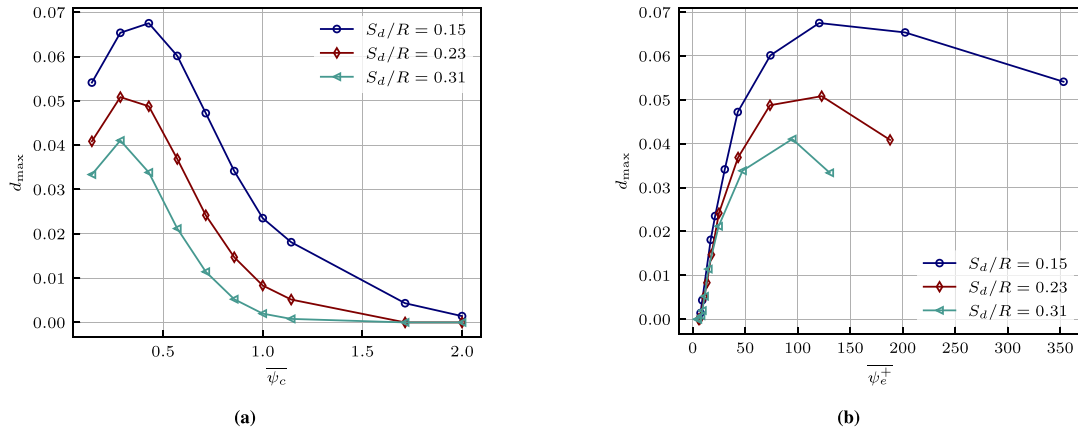

(a)

(b)

Fig. 18. Sensitivity of the damage field on the surface of the solid domain in response to variations in the nucleation energy ψ_c. (a) Maximum damage d_{max} as a function of $\overline{\psi_c}$, (b) Maximum damage d_{max} as a function of $\overline{\psi^+}$.

Fig. 17 shows the maximum damage d_{max} and the radial position of the maximum damage $r|_{d=d_{max}}/R$ as a function of $\overline{p_0}$ for three different standoff distances. As in the previous subsection, we use $\overline{\psi_c}$ to denote the magnitude of the nucleation energy relative to the baseline value provided in Table 1.

Some aspects of the results shown in Fig. 18 are intuitive while others are not. We draw attention first to Fig. 18(a) and the portion of the curves where $\overline{\psi_c} > 1$. These results correspond to the use of nucleation energies that are larger than the baseline in Table 1. Here, the results are as expected: as the nucleation energy is increased, the maximum damage decreases. Eventually, at some point the threshold is sufficiently large such that little to no damage develops, regardless of the proximity of the point source to the surface.

We now focus on the portion of the plots in Fig. 18(a) corresponding to values of the nucleation energy below that in Table 1.

In the range where $0.5 \leq \overline{\psi_c} < 1$, the response is once again as expected. A lower threshold for damage leads to the maximum damage increasing for all three standoff distances. However, this trend does not continue in the range where $0.0 \leq \overline{\psi_c} < 0.5$. One might expect all the curves to peak as $\overline{\psi_c} \rightarrow 0$, but this is not the case. Instead the maximum damage exhibits a local peak and then decreases as $\overline{\psi_c}$ approaches zero. The results are a reflection of the fact that the maximum damage on the surface is only one indicator of the damage response in the solid domain. In Fig. 19, we examine the full damage fields for $\overline{\psi_c} = 0.14$ and $\overline{\psi_c} = 0.43$ at $S_d/R = 0.15$. As can be seen by comparing the two plots, the smaller threshold clearly gives rise to much more damage throughout the domain, even though the maximum damage is below that obtained for the larger threshold.

As the pressure is increased in magnitude, the maximum damage increases, as expected. Moreover, as the magnitude of the acoustic source is increased, the location of the maximum damage eventually moves closer to the center of the domain. This is a similar effect to decreasing the standoff distance alone, as in both cases points on the solid surface closer to the center of the domain experience a larger effective pressure.

5.4.2. Influence of material properties

Next, we examine how the damage that develops in the solid domain is sensitive to changes in the material properties, in particular, to the nucleation energy ψ_c and the critical energy release rate $\mathcal{G}_c$.

In the results that follow, to help illustrate the influence of the material properties on the resulting damage, we define the normalized maximum "tensile" strain energy as

$$\overline{\psi^+} := \frac{\max\{\psi^+\} - \psi_c}{\psi_c}.$$

This quantity provides an indicator of how much greater the driving force for fracture is relative to the threshold value ψ_c. For example, a negative value of $\overline{\psi^+}$ corresponds to $\max\{\psi^+\} < \psi_c$, which means that damage will not initiate.

We begin by studying the influence of the nucleation energy on the resulting damage profile after a single acoustic pulse. Fig. 18 shows the maximum damage d_{max} as a function of $\overline{\psi_c}$ and $\overline{\psi^+}$ for three different
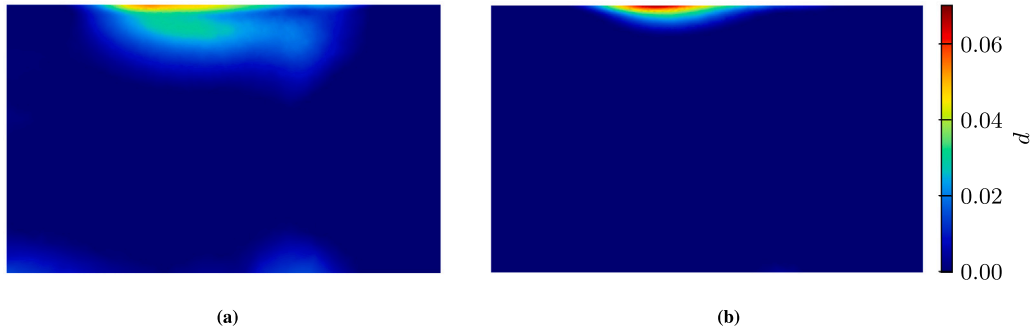
(a)　　　　　　　　　　　　　**(b)**

Fig. 19. Contour plot of the damage field over the solid domain for different nucleation energies at the standoff distance $S_d/R = 0.15$. (a) $\overline{\psi_c} = 0.14$, (b) $\overline{\psi_c} = 0.43$.
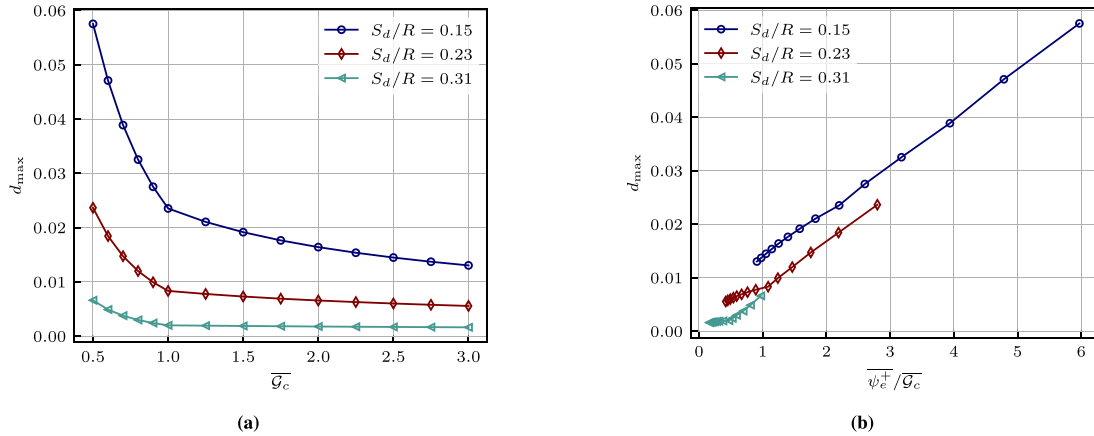

(a)　　　　　　　　　　　　　**(b)**

Fig. 20. Sensitivity of the damage field on the surface of the solid domain in response to variations in the critical energy release rate $\mathcal{G}_c$. (a) Maximum damage $d_{\max}$ over varying $\overline{\mathcal{G}_c}$, (b) Maximum damage $d_{\max}$ over varying $\overline{\psi^+}/\overline{\mathcal{G}_c}$.

The above explanation also aids in the interpretation of the results shown in Fig. 18(b). Recall that $\overline{\psi^+}$ is a measure of how much larger the "tensile" strain energy is relative to ψ_c. Larger values of $\overline{\psi^+}$ correspond to smaller values of ψ_c. The results for $0 \leq \overline{\psi^+} < 40$ indicate that the maximum damage nearly scales linearly with $\overline{\psi^+}$ for all three standoff distances. But the maximum damage once again does not increase monotonically as the threshold ψ_c continues to be lowered and the relative magnitude $\overline{\psi^+}$ of the "tensile" strain energy increases.

Finally, we examine how variations in the critical energy release rate $\mathcal{G}_c$ of the solid impact the maximum damage magnitude, for several standoff distances. We examine the sensitivity of the damage in response to a range of the critical energy release rate corresponding to $\overline{\mathcal{G}_c} \in [0.5, 3.0]$. Fig. 20 shows the maximum damage $d_{\max}$ as a function of $\overline{\mathcal{G}_c}$ and $\overline{\psi^+}/\overline{\mathcal{G}_c}$ for three different standoff distances. As the critical energy release rate is increased, the maximum damage decreases, as expected. Moreover, Fig. 20(b) shows that the maximum damage almost increases linearly with $\overline{\psi^+}/\overline{\mathcal{G}_c}$ for all three standoff distances considered.

5.4.3. Multi-pulse response and limiting cases

The NPL experiments on BegoStone reported in Yang (2018) indicate that in most cases, very little damage is observed on the surface of the solid after a single pulse. At small standoff distances, however, macroscale cracks were observed to form after a sufficient number of pulses. In a damage-based model such as the one used in this work, macroscopic cracks correspond to damage zones that are localized and have reached their peak value of $d = 1$. In the results reported in the previous sections, the maximum damage value after a single pulse was generally observed to be well below 1.0. Indeed, among all of the parameter studies conducted, the maximum damage predicted by the model after a single pulse was approximately $d_{\max} = 0.33$.
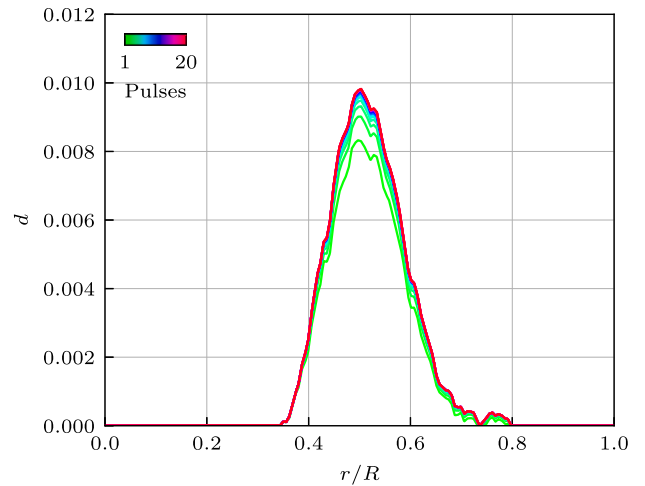

Fig. 21. Variation of the damage profiles for a 20-pulse simulation for $S_d/R = 0.23$ on the top surface of the solid.

Fig. 21 shows the damage profiles along the surface of the solid after multiple pulses (number of pulses $\in [1, 20]$), using the baseline material properties provided in Table 1. The damage magnitude keeps increasing after the first 10 pulses, and then saturates at $d \approx 0.01$. These results indicate that in order to capture the formation of macroscopic cracks, the model needs to be modified in some manner.

One approach would be to include a fatigue-type mechanism in the model that would degrade the fracture resistance as a function of loading history. Models aimed at describing this effect have been
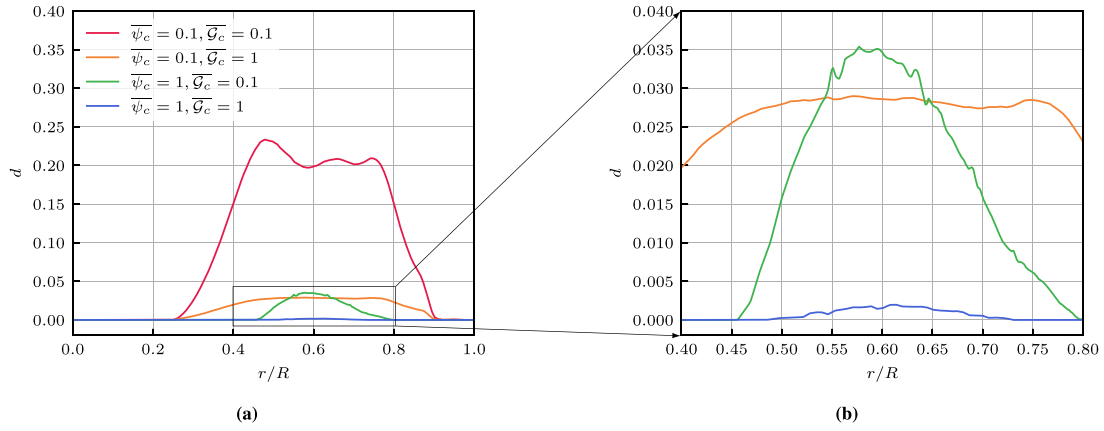
Fig. 22. (a) Variation of the maximum damage for limiting cases that ψ_c and $\mathcal{G}_c$ are degraded, for $S_d/R = 0.31$ on the top surface of the solid. (b) Zoom plot of (a).

proposed for gradient damage based methods, such as in Peerlings et al. (2000), da Costa Mattos (2017), Luo et al. (2020). Most of these models have looked to degrade the critical energy release rate $\mathcal{G}_c$ with load history, as opposed to the threshold for damage. In what follows, we examine some limiting cases with the current model to shed insight into model development for this class of problems.

In particular, we now examine several limiting cases in which either the critical energy release rate $\mathcal{G}_c$ or the nucleation energy ψ_c (or both) are reduced to 10% of their baseline value, while keeping all other parameters fixed.

In Fig. 22, we plot the simulated damage profiles along the top surface of the solid for four limiting cases: (a) base case $\overline{\psi_c} = 1, \overline{\mathcal{G}_c} = 1$, (b) $\mathcal{G}_c$, $\overline{\psi_c} = 1, \overline{\mathcal{G}_c} = 0.1$, (c) ψ_c, $\overline{\psi_c} = 0.1, \overline{\mathcal{G}_c} = 1$, and (d) $\overline{\psi_c} = 0.1, \overline{\mathcal{G}_c} = 0.1$.

When only the critical energy release rate $\mathcal{G}_c$ is decreased (compare blue and green curves in Fig. 22), the damage magnitude is observed to increase significantly, but the damaged area remains approximately the same. When only ψ_c is decreased (compare blue and orange curves in Fig. 22), both the damage magnitude and the size of the damaged region increase. However, in both of the above cases, the maximum damage does not exceed 5%, which is far from full localization. By comparison, the damage magnitude reaches a much larger value when both ψ_c and $\mathcal{G}_c$ are degraded, as case (d), the red line in Fig. 22(a) illustrates.

5.5. A first step to develop a low-cycle fatigue damage model

In the following, aspects of the phase-field for fracture with fatigue models proposed by Carrara et al. (2020) and Grossman-Ponemon et al. (2022) are adapted to the current setting to illustrate a possible means to capture damage localization in response to multiple pulses in NPL.

We begin by defining the history state variable

$$\overline{\alpha}(\boldsymbol{x}, t) = \int_0^t \mathcal{H}\left(\dot{\alpha}(\boldsymbol{x}, \tau)\right) \alpha(\boldsymbol{x}, \tau) \, d\tau \quad \text{with} \quad \alpha(\boldsymbol{x}, t) = \left\langle \psi^+\left(\boldsymbol{\varepsilon}(\boldsymbol{u})\right) - \psi_c^0 \right\rangle_+, \tag{25}$$

where $\mathcal{H}$ stands for the Heaviside function and ψ_c^0 stands for a reference nucleation energy. The definition (25) specifies that the state variable $\overline{\alpha}$ only increases when the "tensile" strain energy ψ^+ is both increasing in time and greater than the reference threshold ψ_c^0.

In contrast to the analogous history state variables in Carrara et al. (2020), the use of the reference threshold ψ_c^0 implies that there are some loadings that, while tensile, are too small to result in any increase in $\overline{\alpha}$. Another difference is that in the current work, the state variable $\overline{\alpha}$ is a measure of accumulated power as opposed to accumulated energy.

As elaborated in Section 5.4.3, model-based simulations indicate that damage localization ($d = 1$) will not occur under repeated pulses unless both the fracture threshold ψ_c and the critical energy release rate $\mathcal{G}_c$ are degraded. Therefore, we propose to view ψ_c and $\mathcal{G}_c$ not as constants but as functions of the loading history of the form

$$\psi_c = f(\overline{\alpha})\psi_c^0 \quad \text{and} \quad \mathcal{G}_c = f(\overline{\alpha})\mathcal{G}_c^0,$$

where $f(\overline{\alpha})$ is a monotonically decreasing function of its argument and where $\mathcal{G}_c^0$ stands for the initial critical energy release rate of the solid. For illustration purposes, similar to Alessi et al. (2018), we consider the degradation function

$$f(\overline{\alpha}) = \begin{cases} 1 & \text{if } \overline{\alpha} \leq \alpha_T \\ (1-k)\left(\dfrac{2\alpha_T}{p\overline{\alpha} + (2-p)\alpha_T}\right)^2 + k & \text{if } \overline{\alpha} \geq \alpha_T, \end{cases}$$

where α_T represents a fatigue threshold, p controls the degradation speed, and k denotes the residual ratio.

In what follows, we set $k = 0.02$, such that at most 98% of the fracture toughness and damage threshold are decreased as a function of repeated loadings.

Fig. 23 shows the damage profiles along the solid surface after multiple pulses using the proposed low-cycle fatigue damage model with two choices of fatigue degradation functions. In Fig. 23(a), we set $p = 0.4, k = 0.02$, and $\alpha_T = 0.02$ so that $f(\overline{\alpha}) \approx 0.1$ at $\overline{\alpha}/\alpha_T = 10$ (after 10 pulses). It can be observed that the peak damage increases relatively slowly in the first 10 pulses, and finally asymptotes to 1 after 25 pulses.

Fig. 23(b) illustrates that by increasing the parameter p to $p = 1$, the damage magnitude increases faster and reaches 1 after 20 pulses. In principle, it seems clear that the incorporation of fatigue effects leads to a model that could be calibrated against experimental observations of fracture in NPL experiments, such as those reported in Yang (2018).

6. Summary and final comments

In this work, a model-based simulation framework for coupled acoustics, linear elastodynamics, and damage is developed for a solid body immersed in a fluid domain, in which a cohesive-type phase field model is employed to characterize the initiation and propagation of fracture in the solid. The interactions between the acoustic waves in the fluid and the solid are enforced by interfacial conditions.

The developed model-based simulation framework is seen to yield reasonable results of wave propagation in the fluid domain, as well as of elastodynamics and damage evolution in the solid domain, when compared to experiments and other simulation results reported in the literature. The simulations illustrate that the wave interaction at the
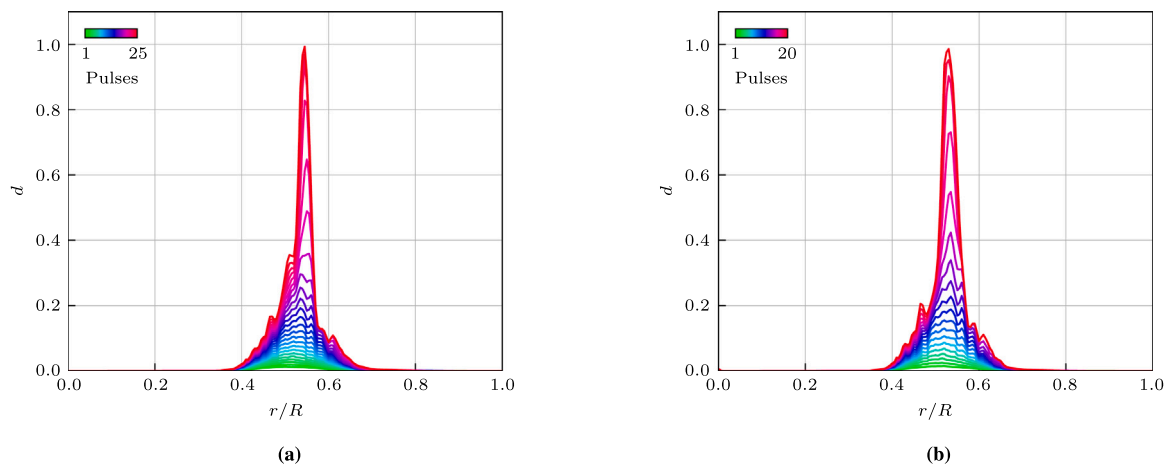
Fig. 23. Variation of the damage profiles for multi-pulse simulation with fatigue for $S_d/R = 0.23$ on the top surface of the solid domain. (a) $p = 0.4, k = 0.02$, (b) $p = 1, k = 0.02$.

fluid–solid boundary generates the surface acoustic waves (the so-called leaky Rayleigh waves) that finally initiate the fracture along the top surface of the solid. The parametric study on the driving forces (the strength of the acoustic point source and the standoff distance from the solid) and the material properties (the nucleation energy and the critical energy release rate) reveal the fundamental fracture mechanisms of the solid and help elucidate differences between the simulation results and the experimental observations.

Although the low-cycle fatigue model proposed in this work allows for qualitatively good comparisons to experimental observations, it is largely a proof-of-concept. Future work will focus on developing a fatigue model that is general and hence capable of describing the full spectrum of experimental observations. In terms of the coupled model, future work will focus on three-dimensional simulations of NPL problems involving samples with initial flaws on the surface, such as those described in Zhang et al. (2017).

CRediT authorship contribution statement

Yangyuanchen Liu: Conceptualization, Formal analysis, Investigation, Software, Writing – original draft. **Pei Zhong:** Conceptualization, Funding acquisition, Writing – review & editing. **Oscar Lopez-Pamies:** Conceptualization, Methodology, Writing – original draft, Writing – review & editing. **John E. Dolbow:** Conceptualization, Funding acquisition, Investigation, Methodology, Project administration, Supervision, Writing – original draft, Writing – review & editing.

Declaration of competing interest

The authors declare that they have no known competing financial interests or personal relationships that could have appeared to influence the work reported in this paper.

Data availability

Data will be made available on request.

Acknowledgments

References

Alessi, R., Ulloa, J., 2023. Endowing Griffith's fracture theory with the ability to describe fatigue cracks. Eng. Fract. Mech. 109048.

Alessi, R., Vidoli, S., De Lorenzis, L., 2018. A phenomenological approach to fatigue with a variational phase-field model: The one-dimensional case. Eng. Fract. Mech. 190, 53–73.

Ambrosio, L., Tortorelli, V.M., 1990. Approximation of functionals depending on jumps by elliptic functionals via γ-convergence. Comm. Pure Appl. Math. 43 (8), 999–1036.

Ambrosio, L., Tortorelli, V.M., 1992. On the approximation of free discontinuity problems. Boll. dell'Unione Mat. Italiana 6-B, 105–123.

Barsoum, R.G.S., 2015. Elastomeric Polymers with High Rate Sensitivity: Applications in Blast, Shockwave, and Penetration Mechanics. William Andrew.

Bourdin, B., Francfort, G.A., Marigo, J.-J., 2000. Numerical experiments in revisited brittle fracture. J. Mech. Phys. Solids 48 (4), 797–826.

Bourdin, B., Francfort, G.A., Marigo, J.J., 2008. The variational approach to fracture. J. Elasticity 91 (1–3), 5–148.

Broda, D., Staszewski, W.J., Martowicz, A., Uhl, T., Silberschmidt, V.V., 2014. Modelling of nonlinear crack–wave interactions for damage detection based on ultrasound—A review. J. Sound Vib. 333 (4), 1097–1118.

Carrara, P., Ambati, M., Alessi, R., De Lorenzis, L., 2020. A framework to model the fatigue behavior of brittle materials based on a variational phase-field approach. Comput. Methods Appl. Mech. Engrg. 361, 112731.

Chen, M., McCauley, J.W., Hemker, K.J., 2003. Shock-Induced localized amorphization in boron carbide. Science 299 (5612), 1563–1566, Publisher: American Association for the Advancement of Science.

Cleveland, R.O., Sapozhnikov, O.A., 2005. Modeling elastic wave propagation in kidney stones with application to shock wave lithotripsy. J. Acoust. Soc. Am. 118 (4), 2667–2676.

Courant, R., Friedrichs, K., Lewy, H., 1928. Über die partiellen differenzengleichungen der mathematischen physik [on the partial difference equations of mathematical physics]. Math. Ann. 100 (1), 32–74.

da Costa Mattos, H.S., 2017. Modelling low-cycle fatigue tests using a gradient-enhanced continuum damage model. Int. J. Damage Mech. 26 (8), 1242–1269.

De Lorenzis, L., Maurini, C., 2021. Nucleation under multi-axial loading in variational phase-field models of brittle fracture. Int. J. Fract..

Ebna Hai, B.S.M., Bause, M., Kuberry, P., 2019. Modeling and simulation of ultrasonic guided waves propagation in the fluid-structure domain by a monolithic approach. J. Fluids Struct. 88, 100–121.

Francfort, G., Marigo, J.-J., 1998. Revisiting brittle fracture as an energy minimization problem. J. Mech. Phys. Solids 46 (8), 1319–1342.

Geelen, R.J., Liu, Y., Hu, T., Tupek, M.R., Dolbow, J.E., 2019. A phase-field formulation for dynamic cohesive fracture. Comput. Methods Appl. Mech. Engrg. 348, 680–711.

Griffith, A.A., 1921. The phenomena of rupture and flow in solids. Phil. Trans. R. Soc. A 221, 163–198.

Grossman-Ponemon, B.E., Mesgarnejad, A., Karma, A., 2022. Phase-field modeling of continuous fatigue via toughness degradation. Eng. Fract. Mech. 264, 108255.

Heister, T., Wheeler, M.F., Wick, T., 2015. A primal-dual active set method and predictor-corrector mesh adaptivity for computing fracture propagation using a phase-field approach. Comput. Methods Appl. Mech. Engrg. 290, 466–495.

Hillerborg, A., Modéer, M., Petersson, P.E., 1976. Analysis of crack formation and crack growth in concrete by means of fracture mechanics and finite elements. Cem. Concr. Res. 6 (6), 773–781.

de Hoop, A.T., van der Hijden, J.H.M.T., 1984. Generation of acoustic waves by an impulsive point source in a fluid/solid configuration with a plane boundary. J. Acoust. Soc. Am. 75 (6), 1709–1715.

Kaplan, A.G., Chen, T.T., Sankin, G., Yang, C., Dale, J.A., Simmons, W.N., Zhong, P., Preminger, G.M., Lipkin, M.E., 2016. Comparison of the nanopulse lithotripter to the holmium laser: Stone fragmentation efficiency and impact on flexible ureteroscope deflection and flow. J. Endourol. 30 (11), 1150–1154.

Kinsler, L.E., Frey, A.R., Coppens, A.B., Sanders, J.V., 1999. Fundamentals of Acoustics. Wiley-VCH, p. 560.

Kumar, A., Bourdin, B., Francfort, G.A., Lopez-Pamies, O., 2020. Revisiting nucleation in the phase-field approach to brittle fracture. J. Mech. Phys. Solids 42, 104027.

Kumar, A., Ravi-Chandar, K., Lopez-Pamies, O., 2022. The revisited phase-field approach to brittle fracture: Application to indentation and notch problems. Int. J. Fract. 237, 83–100.

Li, B., Pandolfi, A., Ortiz, M., 2015. Material-point erosion simulation of dynamic fragmentation of metals. Mech. Mater. 80, 288–297.

Li, H., Zhou, Z., 2019. Numerical simulation and experimental study of fluid-solid coupling-based air-coupled ultrasonic detection of stomata defect of lithium-ion battery. Sensors (Basel, Switzerland) 19 (10).

Lingeman, J.E., McAteer, J.A., Gnessin, E., Evan, A.P., 2009. Shock wave lithotripsy: Advances in technology and technique. Nat. Rev. Urol. 6 (12), 660–670, Number: 12 Publisher: Nature Publishing Group.

Liu, Y., Zhong, P., 2002. BegoStone - A new phantom for shockwave lithotripsy research. J. Acoust. Soc. Am. 112 (4).

Lorentz, E., 2017. A nonlocal damage model for plain concrete consistent with cohesive fracture. Int. J. Fract. 207 (2), 123–159.

Lorentz, E., Cuvilliez, S., Kazymyrenko, K., 2011. Convergence of a gradient damage model toward a cohesive zone model. C. R. Méc. 339 (1), 20–26.

Luo, Z., Chen, H., Zheng, R., Zheng, W., 2020. A damage gradient model for fatigue life prediction of notched metallic structures under multiaxial random vibrations. Fatigue Fract. Eng. Mater. Struct. 43 (9), 2101–2115.

Miehe, C., Welschinger, F., Hofacker, M., 2010. Thermodynamically consistent phase-field models of fracture: Variational principles and multi-field FE implementations. Internat. J. Numer. Methods Engrg. 83 (10), 1273–1311.

Peerlings, R.H.J., Brekelmans, W.a.M., de Borst, R., Geers, M.G.D., 2000. Gradient-enhanced damage modelling of high-cycle fatigue. Internat. J. Numer. Methods Engrg. 49 (12), 1547–1569.

Permann, C.J., Gaston, D.R., Andrš, D., Carlsen, R.W., Kong, F., Lindsay, A.D., Miller, J.M., Peterson, J.W., Slaughter, A.E., Stogner, R.H., Martineau, R.C., 2020. MOOSE: Enabling massively parallel multiphysics simulation. SoftwareX 11, 100430.

Ramirez, B.J., Gupta, V., 2018. Evaluation of novel temperature-stable viscoelastic polyurea foams as helmet liner materials. Mater. Des. 137, 298–304.

Rice, J.R., 1980. The mechanics of earthquake rupture. In: Dziewonski, A., Boschi, E. (Eds.), Physics of the Earth's Interior. pp. 555–649.

Tanguay, M., Colonius, T., 2003. Progress in modeling and simulation of shock wave lithotripsy (SWL). p. 11.

Tham, L.M., Lee, H.P., Lu, C., 2007. Enhanced kidney stone fragmentation by short delay tandem conventional and modified lithotriptor shock waves: A numerical analysis. J. Urol. Publisher: Wolters KluwerPhiladelphia, PA.

Wang, C.C., Truesdell, C., 1973. Introduction to Rational Elasticity. Noordhoff International.

Weinberg, K., Ortiz, M., 2009. Kidney damage in extracorporeal shock wave lithotripsy: A numerical approach for different shock profiles. Biomech. Model. Mechanobiol. 8 (4), 285–299.

Yang, C., 2018. Mechanisms of Stone Fragmentation Produced by Nano Pulse Lithotripsy (NPL) (Ph.D. thesis). Duke University.

Zhang, Y., Yang, C., Liao, D., Zhong, P., 2017. Interaction between lithotripsy-induced surface acoustic waves and pre-existing cracks. J. Acoust. Soc. Am. 141 (5), 3673, Publisher: Acoustical Society of America.

Zhang, Y., Yang, C., Qiang, H., Zhong, P., 2019. Nanosecond shock wave-induced surface acoustic waves and dynamic fracture at fluid-solid boundaries. Phys. Rev. Res. 1 (3), 033068.

Zhong, P., 2013. Shock wave lithotripsy. In: Delale, C.F. (Ed.), Bubble Dynamics and Shock Waves. In: Shock Wave Science and Technology Reference Library, Springer, Berlin, Heidelberg, pp. 291–338.